



Università degli Studi di Ferrara

Corso di Laurea in
Master's Degree in Physics

*Characterization of the components of the
Ring-Imaging CHerenkov detector of the
CLAS12 experiment*

Relatore: Prof. Paolo Lenisa

Correlatore: Dott. Marco Contalbrigo

Laureando:
Giorgio Battaglia

Anno Accademico 2013-2014

Contents

1	Physical motivations	5
1.1	The spin of the nucleus	6
1.2	Deep inelastic scattering	7
1.3	Semi-Inclusive Deep inelastic scattering	10
1.4	Probing strangeness	16
2	The Jefferson Lab	19
2.1	The Facility	20
2.1.1	The Jefferson Lab	20
2.1.2	The Continuous Electron Beam Accelerator Facility	20
2.1.3	The Experimental Halls	22
2.2	The CLAS12 Detector	25
2.2.1	The Superconducting Magnets	26
2.2.2	The Silicon Vertex Tracker	28
2.2.3	The Drift Chambers	29
2.2.4	The Time of Flight	30
2.2.5	The High Threshold Cherenkov Counter	31
2.2.6	The Low Threshold Cherenkov Counter	32
2.2.7	The Preshower Calorimeter	33
3	The CLAS12 RICH	35
3.1	The Cherenkov effect	35
3.2	The number of photons and detections resolution	37
3.3	Cherenkov detectors	39
3.3.1	The Threshold Cherenkov Detectors	39
3.3.2	The Differential Cherenkov Detectors	39
3.3.3	The Ring Imaging Cherenkov	40
3.4	The CLAS12 RICH	42

3.4.1	The Aerogel Radiator	44
3.4.2	The Photon Detectors	45
3.4.3	The Focusing System	47
4	Single Photon Resolution	51
4.1	Emission Point Contribution	51
4.2	Chromatic Aberrations	52
4.3	Readout Accuracy	52
4.4	Focusing System Resolution	53
4.5	Mirror $\sigma_{\theta_{Ch}}$ contribution	54
4.6	Aerogel $\sigma_{\theta_{Ch}}$ contribution	56
5	Aerogel Characterization Measurement	59
5.1	Touching Machine Measurement	61
5.2	Laser Reflection Measurement	65
5.3	X-ray Measurement	73
6	Mirror Characterization Measurement	79
6.1	Mirror Measurement	80
6.2	Planar Mirror Measurement	87
6.3	Aerogel-Mirror Measurement	88
7	Conclusion	93
A	Large Area Picosecond PhotoDetector	95

Abstract

One of the purposes of the CLAS12 experiment at Jefferson Lab, Newport News, VA USA, is to study the 3D nucleon structure in the yet poorly explored valence region by deep-inelastic scattering, and to perform precision measurements in hadronization and hadron spectroscopy. The CLAS12 Ring Imaging Cherenkov detector (RICH) is designed for hadron identification in the momentum range between 3 and 8 GeV/c. It is a double configuration detector. The radiator is made of aerogel tiles. The Cherenkov radiation emitted in the forward region (polar angle $\theta < 13^\circ$) will be collected directly by the PMTs. Photons produced at larger incident angles ($13^\circ < \theta < 35^\circ$) will reach the PMTs after being focused by a spherical mirror and then reflected by a planar one while passing twice the radiator. One of the main estimator of the RICH performance is the single photon resolution $\sigma_{\theta_{Ch}}$. There are several factor contributing to the total resolution: emission point, chromatic aberration, readout and focusing system accuracy. The total effect is the square sum of all the factor. The focusing system contribution can be decomposed as: $\sigma_{\theta_{Ch}}^{focus} = \sqrt{(\sigma_{\theta_{Ch}}^{spherical})^2 + (\sigma_{\theta_{Ch}}^{aerogel})^2 + (\sigma_{\theta_{Ch}}^{planar})^2}$. This thesis work is mainly related to the focusing system contribution to the the RICH photon resolution. It will be presented an upper limit for the RMS of the angular distribution of the normal to the aerogel surface θ_{aer} suitable for aerogel characterization. This upper limit can be measured with a non invasive laser reflection setup that will be then described. Finally it will be shown the results of several mirror stress test.

Chapter 1

Physical motivations

1.1 The spin of the nucleus

The spin was discovered for the first time during the studies of the atomic spectra. It was proposed in 1924 from Wolfgang Pauli as two-valued quantum degree of freedom. At the beginning it was interpreted as self-rotation of the electron, but this idea was severely criticized by Pauli. Nowadays we know the spin is an intrinsic form of angular momentum of elementary particles (quarks and leptons) and of all the particles composed by them (hadrons and nuclei).

The important question today is: how the nucleon spin is carried by his constituents?

Before 1980s it was expected that the nucleon spin was carried by the valence quarks, but the results of EMC experiment contradicted these expectations [1]. Indeed, considering all the possible contribution to the nucleon's spin we can write:

$$\mathbf{s}^N = \frac{1}{2} = \frac{1}{2}\Sigma_q + \Sigma_g + \mathbf{L}_q + \mathbf{L}_g \quad (1.1)$$

where \mathbf{s}^N is the spin of the nucleon, Σ_q is the quark spin component, Σ_g is the gluon spin component and \mathbf{L}_q and \mathbf{L}_g are the orbital angular momentum components of quarks and gluons.

The COMPASS and HERMES collaborations found that the Σ_q contribution of the proton spin is only 30% of the total [2].

At present time we can have informations on the three-dimensional nucleon structure only by phenomenological structure functions. The GPDs, Generalized Parton Distribution, describe the nucleon in the longitudinal momentum and 2D transverse position space, instead the TMD, Transverse Momentum Dependent Probability Distribution Function, describe the distribution in the momentum space.

1.2 Deep inelastic scattering

The principal way to study the internal structure of the nucleons are scattering experiments. A very common technique is the Deep Inelastic Scattering (DIS). In this kind of experiment a lepton (point-like particle) beam scatters off a nucleon target (protons, deuterons, ...). The scattering process can be described as:

$$l(k) + N(P) \rightarrow l'(k') + X. \quad (1.2)$$

where l and l' represent the lepton beam before and after scattering and N the nucleon target. The quantity inside the parenthesis are the respective four-momenta.

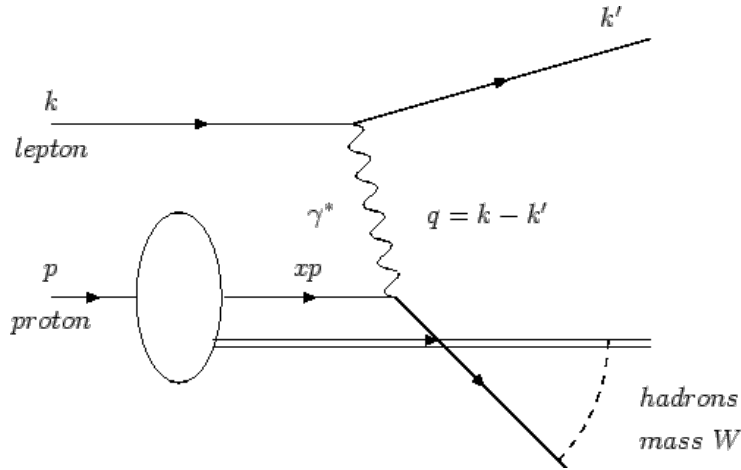


Figure 1.1: the Feynman diagram of DIS in the Born approximation.

The relevant kinematic variables of this process and of further calculations are the Bjorken scaling variable:

$$x_b = \frac{Q^2}{2P \cdot q} = \frac{Q^2}{2M\nu} \quad (1.3)$$

and the exchanged fractional energy

$$y = \frac{\nu}{E}, \quad (1.4)$$

in which P is the four-momentum of the target nucleon, M is the nucleon's rest mass, $\nu = E - E'$ is the virtual photon energy, x_b is the Bjorken scaling variable, y is the fractional energy, E is the beam energy and $Q^2 = -q^2$.

The invariant mass of the photon-nucleon system is:

$$W^2 = (P + q)^2 = M^2 + 2M\nu - Q^2. \quad (1.5)$$

The differential cross section of this interaction is:

$$\begin{aligned} \frac{d\sigma}{dx_b dy d\phi_s} = & \frac{2\alpha^2}{x_b y Q^2} \frac{y^2}{2(1-\varepsilon)} \cdot \\ & \cdot \left[F_T + \varepsilon F_L + S_{\parallel} \lambda_e \sqrt{1-\varepsilon^2} w x_b (g_1 - \gamma^2 g_2) + \right. \\ & \left. - |S_{\perp}| \lambda_e \sqrt{2\varepsilon(1-\varepsilon)} \cos \phi_s 2x_b \gamma (g_1 + g_2) \right], \end{aligned} \quad (1.6)$$

in which we have defined the lepton's helicity λ_e , the target spin vector \mathbf{S} , the spin component transverse and parallel to the photon momentum S_{\perp} and S_{\parallel} , α is the fine structure constant and

$$\varepsilon = \frac{1-y}{1-y+\frac{1}{2}y^2} \quad (1.7)$$

is the ratio of longitudinal and transverse photon flux. The remaining unknown quantity in the cross section formula are the four structure functions (F_T, F_L, g_1, g_2) that depend only on the Bjorken variable x_b and Q^2 .

The Quark Parton Model postulates that nucleons are made of partons, point-like spin 1/2 particles. If we make all the calculations in the "infinite momentum frame" (a reference frame in which the hadrons' momentum is infinitely large) the transverse momentum of the partons is negligible. In a high Q^2 scattering process we can consider the photon absorbed by a single parton and thus we can resolve the partons. In this case x_b , the Bjorken variable, represents the fraction of longitudinal momentum of the nucleon carried by the struck quark. In the QPM the following structure functions relation are valid:

$$F_T = x_b \sum_q e_q^2 f_1^q(x_b) \quad (1.8)$$

$$F_L = 0 \quad (1.9)$$

$$g_1 = \frac{1}{2} \sum_q e_q^2 g_{1L}^q(x_b) \quad (1.10)$$

$$g_2 = 0; \quad (1.11)$$

with e_q the charge of the parton. In the previous equations the only two structure functions that are different from zero depend only on x_b . This fact is called Bjorken scaling. f_1 and g_1 are the so called Probability Density Functions (PDFs). f_1 represents the probability to find inside a proton a quark with a fraction x_b of the proton momentum regardless of its spin polarization. The helicity distribution $g_1(x_b)$ is the difference in probability of finding a quark with spin parallel or antiparallel to the polarization of the nucleus. There exists a third PDF, $h_1(x_b)$, that is analogous to $g_1(x_b)$ but for the transverse case. The scaling behavior is experimentally confirmed only in a small kinematic region, where $x_b \sim 0.2$. In this region, data confirm the Bjorken scaling, but measurements find significant deviations on a wider x_b range. In this region the QPM is not sufficiently adequate. Furthermore PDFs give no information about quark angular momentum.

1.3 Semi-Inclusive Deep inelastic scattering

In semi-inclusive Deep Inelastic Scattering at least a hadron is detected in conjunction with the scattered lepton.

$$l(k) + N(P) \rightarrow l'(k') + h(P_h) + X. \quad (1.12)$$

More variables are required to describe the reaction with respect DIS.

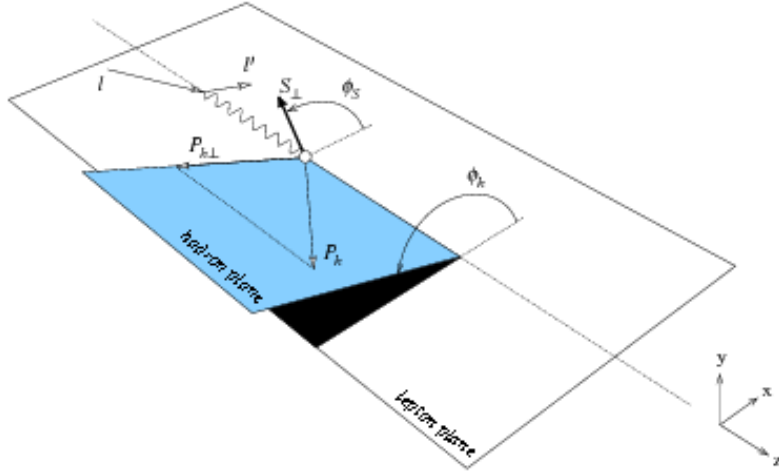


Figure 1.2: The notation of ϕ_h and ϕ_s .

The first is P_T , the transverse momentum of the detected hadron. In terms of the hadron momentum P_h it can be written:

$$P_T = \frac{\vec{q} \cdot \vec{P}_h}{|\vec{q}|}. \quad (1.13)$$

The other variables are the ratio between the energy carried by the detected hadron and the energy of the virtual photon in the nucleon rest reference frame:

$$z = \frac{P \cdot P_h}{P \cdot q}; \quad (1.14)$$

and finally the missing mass W' :

$$W' = \sqrt{(q + P - P_h)^2}. \quad (1.15)$$

The general cross section of the process is:

$$\frac{d^6\sigma}{dx_b dy dz d\phi_s dP_{h\perp}^2} = \frac{\alpha^2 y}{8zQ^4} 2MW^{\mu\nu} L_{\mu\nu} \quad (1.16)$$

where $W^{\nu\mu}$ is the hadronic tensor and $L^{\nu\mu}$ is the leptonic one.


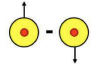
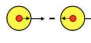
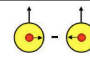


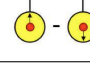
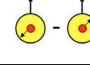
The hadronic tensor of a semi-inclusive deep inelastic scattering process is characterized by eighteen structure functions. The differential cross section in terms of them is:

$$\begin{aligned} & \frac{d^6\sigma}{dx_b dy dz d\phi_s dP_{h\perp}^2} = \\ & \frac{\alpha^2}{x_b y Q^2} \frac{y^2}{2(1-\varepsilon)} \left\{ F_{UU,T} + \varepsilon F_{UU,L} + \sqrt{2\varepsilon(1+\varepsilon)} \cos(\phi_h) F_{UU}^{\cos(\phi_h)} + \right. \\ & \quad + \varepsilon \cos(2\phi_h) F_{UU}^{\cos(2\phi_h)} + \lambda_e \sqrt{2\varepsilon(1-\varepsilon)} \sin(\phi_h) F_{LU}^{\sin(\phi_h)} + \\ & \quad + S_{\parallel} \left(\sqrt{1-\varepsilon^2} F_{LL} + \sqrt{2\varepsilon(1-\varepsilon)} \cos(\phi_h) F_{LL}^{\cos(\phi_h)} \right) + \\ & \quad + S_{\parallel} \lambda_e \left(\sqrt{\varepsilon^2} F_{LL} + \sqrt{2\varepsilon(1-\varepsilon)} \cos(\phi_h) F_{LL}^{\cos(\phi_h)} \right) + \\ & \quad |S_{\perp}| \left[\sin(\phi_h - \phi_s) \left(F_{UT,T}^{\sin(\phi_h + \phi_s)} + \varepsilon F_{UT,L}^{\sin(3\phi_h - \phi_s)} \right) + \right. \\ & \quad \left. + \varepsilon \sin(\phi_h + \phi_s) F_{UT}^{\sin(\phi_h + \phi_s)} + \varepsilon \sin(3\phi_h - \phi_s) F_{UT}^{\sin(3\phi_h - \phi_s)} + \right. \\ & \quad \left. + \sqrt{2\varepsilon(1+\varepsilon)} \sin(\phi_s) F_{UT}^{\sin(\phi_s)} + \sqrt{2\varepsilon(1+\varepsilon)} \sin(2\phi_h - \phi_s) F_{UT}^{\sin(2\phi_h - \phi_s)} \right] + \\ & \quad + |S_{\perp}| \lambda_e \left(\sqrt{1-\varepsilon^2} \cos(\phi_h - \phi_s) F_{LT}^{\cos(\phi_h - \phi_s)} + \sqrt{2\varepsilon(1-\varepsilon)} \cos(\phi_s) F_{LT}^{\cos(\phi_s)} + \right. \\ & \quad \left. + \sqrt{2\varepsilon(1-\varepsilon)} \cos(2\phi_h - \phi_s) F_{LT}^{\cos(2\phi_h - \phi_s)} \right) \left. \right\}. \quad (1.17) \end{aligned}$$

The $F_{U,T,L}$ are structure functions. The index U,T,L means that they are respectively unpolarized, transversely polarized and longitudinally polarized. The factorization theorem allows to factorize the cross section as follows:

$$\frac{d^3\sigma^h}{dx_b dQ^2 dz} = \sum_{a,b=q,\bar{q},g} d_a(x_b, p_T^2) \otimes \sigma_{ab}(x_b, Q^2) \otimes F_b^h(z, Q^2), \quad (1.18)$$

where $d_a(x_b, p_T^2)$ are TMDs that describe the distribution of the parton a inside the nucleon, σ_{ab} is the hard-scattering cross section for the process $la \rightarrow l'b$ (calculable with PQCD) and $F_b^h(z, Q^2)$ describes the fragmentation of the final parton b into a hadron h carrying a fraction of energy z . The TMDs provide a 3D description of the nucleon, since they depend not only on x_b but also on the parton transverse momentum p_T . There are eight TMDs at the Leading Order (LO), categorized by nucleon and quark spin in the following table.

Quark \ Nucleon	Unpolarized	Longitudinal	Transverse
Unpolarized	f_1 		f_{1T}^\perp 
Longitudinal		g_{1L} 	g_{1T} 
Transverse	h_1^\perp 	h_{1L}^\perp 	h_{1T} 
			h_{1T}^\perp 

The symbol f represents the TMD of an unpolarized parton, the symbol g of a longitudinally polarized and h of a transversely polarized parton, respectively. The subscripts L and T refer to the nucleon, if it is longitudinally or transversely polarized. The three TMD on the diagonal (f_1 , g_{1L} , h_{1T}) are the 3D generalization of the PDFs, while the probabilistic description of the other five is the follow:

	name of the function	description
$f_{1T}^\perp(x_b, p_T^2)$	Sivers	Describes the unpolarized quark inside a transversely polarized nucleon [4].
$g_{1T}(x_b, p_t^2)$	Worm-Gear	Describes the distribution of longitudinally polarized quarks in a transversely polarized nucleon.
$h_{1T}^\perp(x_b, p_T^2)$	Pretzelosity	Describes the correlation of quark transverse polarization and momentum in a nucleon with transverse polarization.
$h_{1L}^\perp(x_b, p_T^2)$	Kotzinian-Mulders	Describes the quark transverse polarization along the quark's intrinsic transverse momentum in the longitudinally polarized target.
$h_1^\perp(x_b, p_T^2)$	Boer-Mulders	Describes quark's transverse polarization along the normal to the plane defined by the quark's intrinsic transverse momentum and the nucleon's momentum in the unpolarized target [4].

The structure functions can be written as:

$$F_{UU,T} \sim \sum_q f_1^q \otimes D_1^q \quad (1.19)$$

$$F_{LL} \sim \sum_q e_q^2 g_1^q \otimes D_1^q \quad (1.20)$$

$$F_{UU}^{\cos(2\phi_h)} \sim \sum_q e_q^2 h_1^{\perp q} \otimes H_1^{\perp q} \quad (1.21)$$

$$F_{UL}^{\sin(2\phi_h)} \sim \sum_q e_q^2 h_{1L}^{\perp q} \otimes H_1^{\perp q} \quad (1.22)$$

$$F_{LT}^{\cos(\phi_h - \phi_s)} \sim \sum_q e_q^2 g_{1T}^q \otimes D_1^q \quad (1.23)$$

$$F_{UL,T}^{\sin(\phi_h - \phi_s)} \sim \sum_q e_q^2 f_{1T}^{\perp q} \otimes D_1^q \quad (1.24)$$

$$F_{UT}^{\sin(\phi_h + \phi_s)} \sim \sum_q e_q^2 h_{1T}^q \otimes H_1^{\perp q} \quad (1.25)$$

$$F_{UT}^{\cos(3\phi_h - \phi_s)} \sim \sum_q e_q^2 h_{1T}^{\perp q} \otimes H_1^{\perp q}, \quad (1.26)$$

where \otimes symbol represents the convolution integral over intrinsic p_T and generated during fragmentation k_T transverse momentum of the quark. Usually it is identified with the symbol C and it is defined as:

$$\begin{aligned} C[wfD] &= x_b \sum_q e_q^2 \int d^2\vec{p}_t d^2\vec{k}_T \delta^{(2)}(\vec{p}_T - \vec{k}_t - \vec{P}_{h\perp}/z) \times \\ &\times w(\vec{p}_T, \vec{k}_T) f^q(x_b, p_T^2) D^q(z, k_T^2). \end{aligned} \quad (1.27)$$

The information about the quark transverse momentum are carried by the hadron transverse momentum.

By detecting hadrons that has spin equal zero (such as kaons and pions) it is possible to access only to two FFs. They are D_1 , that represents an unpolarized quark and hadron, and the Collins function H_1^\perp [4] that represents how a transversely polarized quark fragments into an unpolarized hadron.

From an experimental point of view it is easier to measure asymmetries rather than cross section since it reduces the uncertainties on the measurements. An asymmetry is the ratio between the difference of two partial cross section over

the total cross section where most systematics cancel out (at first order). Based on the type of hadron you decide to detect you can enhance the TMD contribution of a given quark. For example, it is possible to gather information on the contribution of the strangeness in the nucleon selecting strange mesons in the detector. This Up to now there are no reason for considering the correlation between momentum and transverse spin, described by the TMDs, been the same for all quark flavors. Therefore it is important to have good particle identification detector in order to distinguish the quark flavor and complete TMDs studies.

1.4 Probing strangeness

Since the strangeness distribution is difficult to determine, a common practice is to use the simplified ansatz $\bar{s} = s = \frac{C_s}{2} (\bar{u} + \bar{d})$. It is based on the absence of significant experimental constraints and on the assumption that, except for a multiplicative factor, the quark \bar{s} contributes as much as the quarks \bar{u} and \bar{d} . [5]

An accurately way to determine the strange distribution is via semi-inclusive experiments.

The HERMES experiment found that the strange distribution is considerably different from the average of the u and d quarks. The collaboration performed a Leading Order extraction of the strange contribution $S = s^+ = s + \bar{s}$ from charged-kaon production in DIS on the deuteron [3]. As we can see in Figure 1.3, the strange distribution deviates significantly from the expectations in the kinematic range close to $x = 0.1$. In the next one, Figure 1.4, you can see a comparison of the distribution of the longitudinal polarized quark s and the sea quarks u and d. One of the purpose of the CLAS12 experiment is to explore in a great detail this kinematic region performing measurements of unprecedented precision.

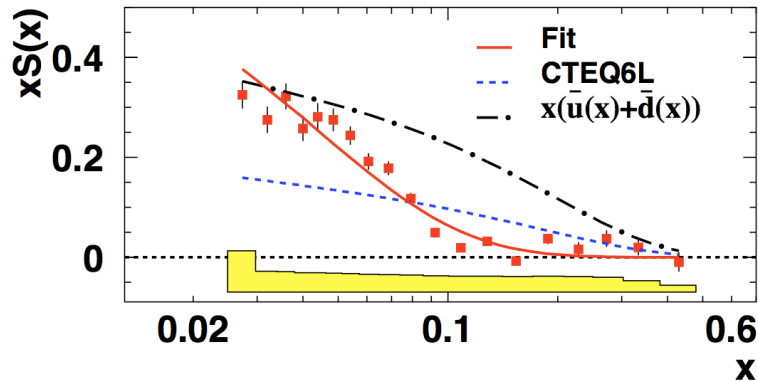


Figure 1.3: The strange distributions $S = s^+ = s + \bar{s}$ extracted in a LO analysis by the HERMES experiment using data from SIDIS kaon production.

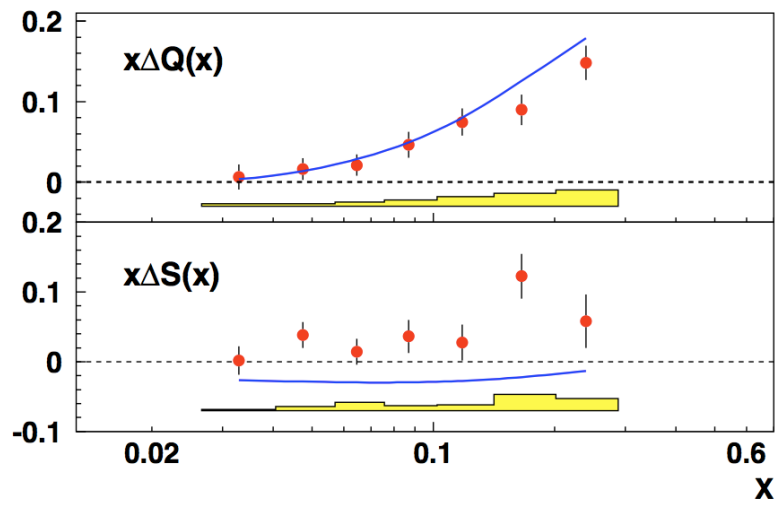


Figure 1.4: The difference between the helicity function for the u-d and the s.

Chapter 2

The Jefferson Lab

2.1 The Facility

2.1.1 The Jefferson Lab



Figure 2.1: The Thomas Jefferson National Accelerator Laboratory.

The Jefferson Lab (JLAB) is a laboratory funded by the U.S. Department of Energy in Virginia (USA). The lab's primary mission is to conduct basic research in nuclear physics using the Continuous Electron Beam Accelerator Facility (CEBAF). Jefferson Lab also conducts a variety of research using the Free-Electron Laser. The X-FEL shares the same electron-accelerating technology used in CEBAF. CEBAF was operating from 1995 to 2012 at the energy of 6 GeV. The Jefferson Lab is upgrading its facilities by doubling the energy of its accelerator's electron beam to 12 GeV. After the 12 GeV upgrade, JLab will host four experimental halls, the already existing Hall A, Hall B and Hall C and the new one Hall D.

2.1.2 The Continuous Electron Beam Accelerator Facility

The CEBAF electron accelerator consists of 1 injector, 2 super-conducting linear accelerator (LINAC) and 2 recirculation arcs. The photocathode gun

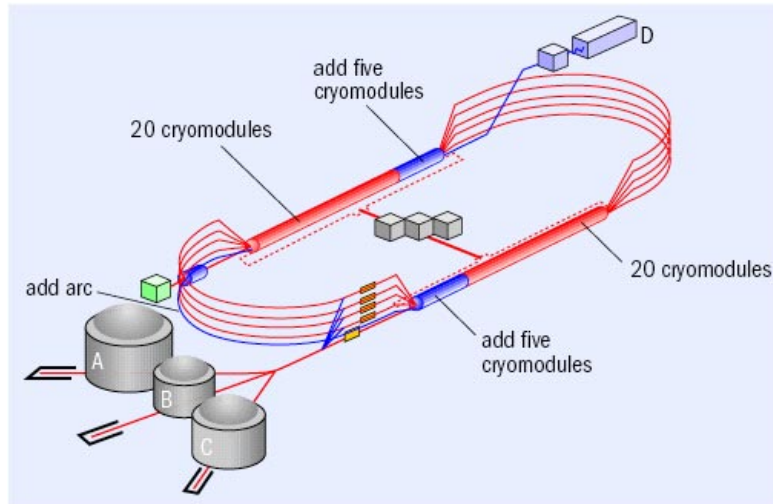


Figure 2.2: The CEBAF upgrade.

system is used to deliver the continuous-wave beams of high polarization and high current. The electron beam obtained has a current of $90\mu A$ for the Hall B and up to $200\mu A$ for the others Halls. The maximum luminosity is $10^{35}\text{cm}^{-2}\text{s}^{-1}$ and the longitudinal polarization of the beam is 85%. This high polarization level is obtained by shining a circularly polarized laser light on a strained gallium arsenide (GaAs) cathode. The beam polarization is measured and monitored by Moeller and Compton polarimeters. After an initial acceleration to 45 MeV, the electrons are injected into the accelerator. Each LINAC can accelerate the electron beam up to about 1 GeV, through radio frequency superconducting cavities. The electrons are accelerated by the LINACS and circulated up to five times. At the end of the recirculation process, the maximum beam energy deliverable to the first three Halls is about 11 GeV, while the energy deliverable to the Hall D is about 12 GeV.

2.1.3 The Experimental Halls

As mentioned before, after the upgrade the Jefferson Lab will host four experimental halls.

Hall A

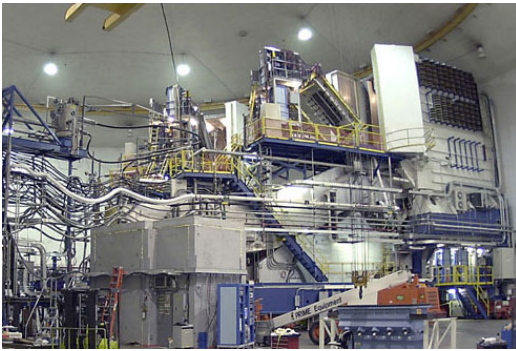


Figure 2.3: One of the two High Resolution Spectrometers in the Hall A.

Hall A is the largest of these four experimental staging areas. It is 53 m across and 25 m tall from the floor to the highest spot on its domed ceiling. The foundation for the hall is 10 m below the ground. Hall A is outfitted with two primary detector systems. They are both high-resolution spectrometers, each weighting about 1.36 t. The hall is used primarily for experiments studying the structure of the nucleus and the protons and neutrons it contains. Hall A experiments focus on nucleon form factors

to high Q^2 , the strange quark structure of the proton, nucleon spin structure, few body form factors to high Q^2 and nuclear structure at small inter-nucleon separations.

Hall B

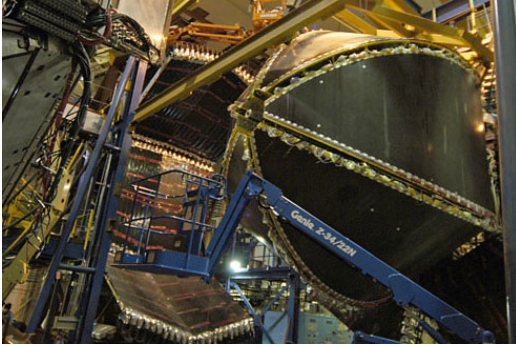


Figure 2.4: A CLAS detector detail from Hall B.

Hall B is the smallest of the experimental staging areas. It is 30 m in diameter and 20 m from floor to ceiling. Experiments taking place in Hall B employ beams of either electrons or photons. From 1995 to 2012, the heart of Hall B physics program involved the use of the CEBAF Large Acceptance Spectrometer (CLAS). This detector system spanned nearly the full angular range around the target and was specifically developed for the study

of exclusive reactions with multiple particles in the final state. In the heart of CLAS was a six-coil superconducting toroid magnet. The detector was instrumented with layers of drift chambers for charged particle tracking, Cherenkov detectors for electron/pion separation, scintillators for time of flight measurements and electromagnetic calorimeters for electron and neutral particle identification. Major research programs in Hall B include experiments to measure the spectrum of excited states of the nucleon to understand nucleon structure and quark confinement, to perform three-dimensional imaging of the quark structure of the nucleon, to characterize nucleon-nucleon correlations in nuclei and to search for the existence of heavy photons. At the present time, the CLAS detector in Hall B has been decommissioned and installation of the new CLAS12 detector is underway. This new large acceptance detector system is part of Jefferson Lab's 12 GeV upgrade and will be used to study hadron structure with unprecedented accuracy.

Hall C

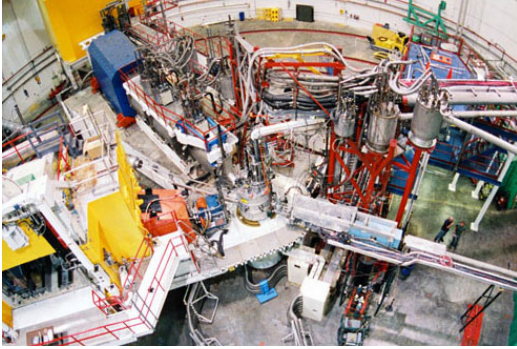


Figure 2.5: An overhead view of Hall C.

and the strangeness content of the nucleons.

Hall C is 45 m in diameter and 19 m tall. Hall C houses a High Momentum Spectrometer and provides space for large installation experiments. These are stand alone experiments requiring unique or highly specialized detectors, magnets and targeting systems. The research equipment in Hall C is used to study the weak charge of the proton, form factors of simple quark systems, the transition from hadrons to quarks

Hall D



Figure 2.6: An overhead view of Hall D.

as exotic or hybrid mesons.

Hall D complex consists of an extension to the accelerator tunnel to house a transport line for the electron beam, which is used to produce a beam of high-energy photons, the experimental hall and its associated detector systems, a counting house, cryogenics plant and service buildings. Experiments to be conducted in Hall D will make it possible for scientists to study what are known

2.2 The CLAS12 Detector

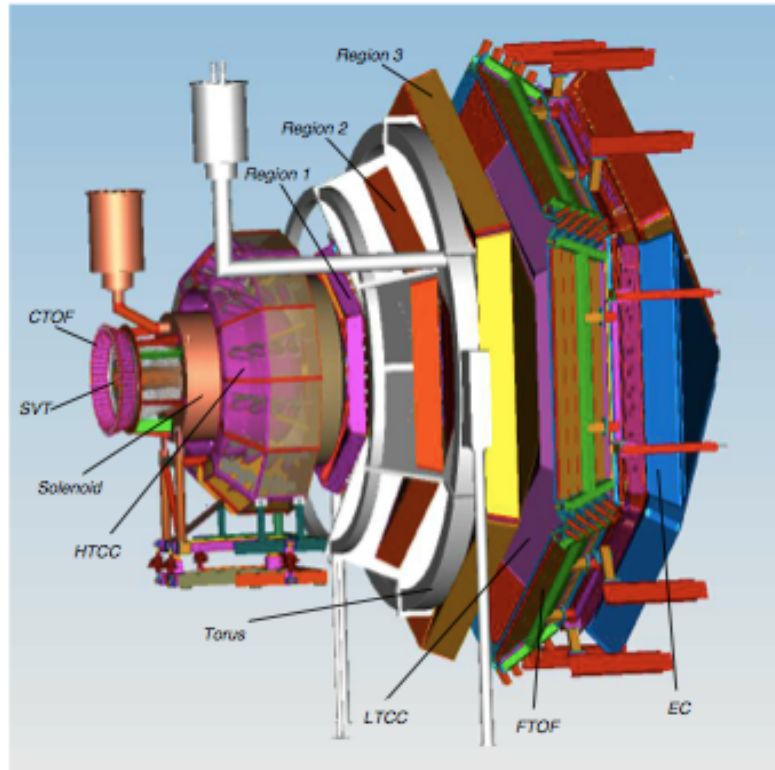


Figure 2.7: The CLAS12 detector.

The Hall B will host the new CLAS12 detector (see Figure 2.7). It will be an upgrade of the previous CLAS detector with improved performances to match the 12 GeV/c requirements. CLAS12 will be a large acceptance spectrometer designed to measure reactions with multi-particle final state and high luminosity using unpolarized or polarized targets. The CLAS12 detector will be divided in two major detectors: a forward detector and a central detector. The forward one will permit to detect forward-going high momentum particles between 5° and 35° of polar angle. The central one will be able to measure particle with a polar angle from 40° to 135° . The geometry of the central detector will allow the use of unpolarized as well as polarized target, of free and bound nuclei.

2.2.1 The Superconducting Magnets

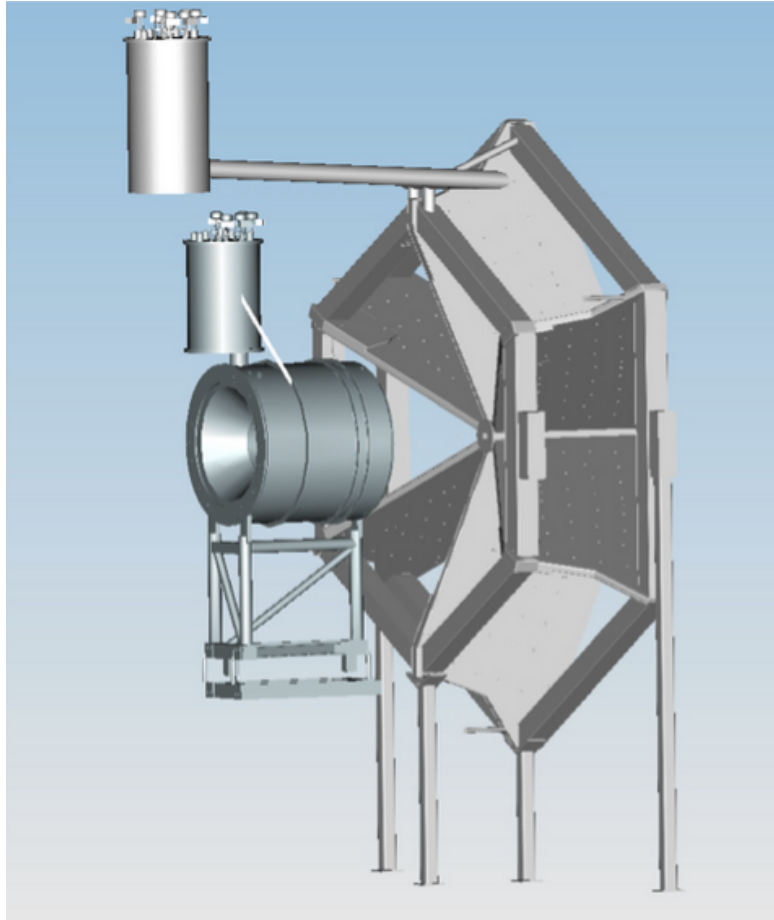


Figure 2.8: The solenoid and torus magnets.

CLAS 12 will contain two superconducting magnets, a six coil torus magnet with a 3.6 T peak field and a 5 T solenoid. The two magnets will provide magnetic analysis of charged particles in the forward range and in the large angle range, respectively. The toroid field drops rapidly with distance and has virtually no impact on the solenoid magnet, and in particular it will not affect the homogeneity of the solenoid magnet in the critical target region. The solenoid field drops more slowly with distance and it will exert a measurable force on the coils of the torus magnet that must be taken into account

in the mechanical design of the magnet.

The Solenoid Magnet

The solenoid magnets will provide an ideal field distribution for the analysis of particle trajectories in the central region, where the bending power of the solenoid is maximum. The choice of a 5 T strong solenoid field has been driven by the necessity of satisfying precise requirements. These requirements include:

- a large opening for charged and neutral particles in the forward hemisphere;
- good charged particle momentum resolution in a limited radial space for polar angles from 35° to 125° and momentum range from 0.3 to 1.3 GeV;
- shielding the sensitive inner detectors against the very high background of Moller electrons;
- operation of a dynamically polarized target ($\frac{\Delta B}{B} < 10^{-4}$);
- high luminosity operation;

The solenoid magnet will provide a strong magnetic field needed for a dynamically polarized solid-state target. At the same time it will be used for particle tracking and momentum analysis.

The Torus Magnet

The torus magnet will be based on six superconducting coils arranged symmetrically around the beam line to generate a field primarily in the azimuthal (ϕ) direction. The choice of this configuration leads to an approximate toroidal field distribution around the beam axis. It has been driven by the necessity of satisfying certain precise physics requirements. Some critical ones are:

- uniform coverage of a large momentum and angle range and symmetry around the axis;

- an open structure that allows for long path lengths for charged and neutral particles (good particle identification through precise time-of-flight measurements);
- low background from electromagnetic processes to reach high luminosity.

The toroid configuration will offer a field-free region around the beam axis and the magnetic field will always be transverse to the particle trajectory (optimal momentum resolution for charged particles). In addition the determination of the azimuthal angle will be decoupled from the measurements of the polar angle and momentum. The six coils have been shaped to give the desired $\int Bdl$ and the requested resolution as a function of θ .

2.2.2 The Silicon Vertex Tracker

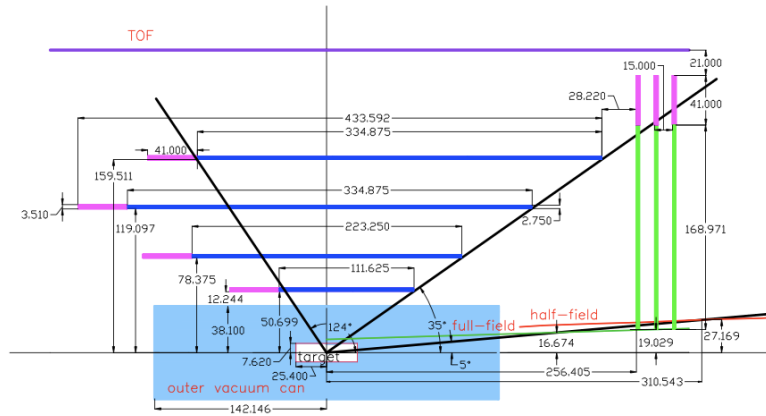


Figure 2.9: Side view of the SVT showing the layout of the barrel and forward regions (all dimensions in mm).

The Silicon Vertex Tracker will consist of two main part: a forward silicon tracker (FST) and a barrel silicon tracker (BST). The first one will cover a polar angular range (θ) between 5° and 35° , while the second between 35° and 125° . The azimuthal coverage (ϕ) will be almost 2π . The SVT will be centered inside the solenoid.

2.2.3 The Drift Chambers

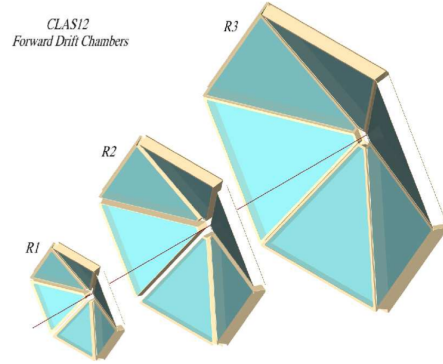


Figure 2.10: Schematic layout of the CLAS12 Forward Drift Chambers.

The overall tracking requirements of the CLAS12 experiment are 0.5 - 1% fractional momentum resolution at 5GeV and efficient tracking at a luminosity of $10^{35} \text{ cm}^{-2} \text{ s}^{-1}$. These are the main constraints for drift chamber design. It was planned to re-use many of the design concepts and most of the utility infrastructure of the CLAS experiment. As shown in Figure 2.10 the forward tracking system consists of three regions: before, inside and outside the torus field volume. Each region is divided in six sectors. All chambers will have its wires arranged in two superlayers of six layers each. The cell will have an hexagonal structure. This means that each sense wire will be surrounded by six field wires. The arrangement will be similar to the previous CLAS design and will offer good resolution with very good pattern recognition properties.

2.2.4 The Time of Flight

Central Time of Flight

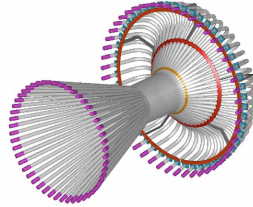


Figure 2.11: The Central Time of Flight detector.

The CTOF system will be part of the Central Detector used for identification of charged particles (PID) emerging from the target via their time of flight. The CTOF system will include 48 plastic scintillators with double-sided photomultiplier (PMT) readout via 1m long upstream and 1.6m long downstream focusing light guides respectively. The array of 48 counters will form an hermetic barrel around the target. The barrel is aligned with the beam axis inside the 5T solenoid. The PMTs will be placed in the region of 1000G fringe field of the solenoid and enclosed into the triple dynamical magnetic shield that provides 0.2G internal PMT field. The CTOF system will be required to have 60 ps timing resolution for particle identification.

Forward Time of Flight

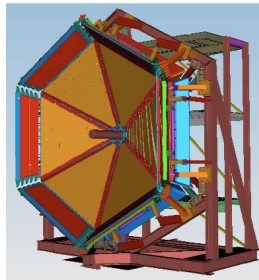


Figure 2.12: The Forward Time of Flight detector.

The FTOF system will be part of the forward detector and used to measure the time of flight of charged particles emerging from the target. The

FTOF system will include 6 sectors of plastic scintillators with double-sided PMT readout. The system is required to have excellent timing resolution (50 ps) for particle identification and good segmentation for flexible triggering options.

2.2.5 The High Threshold Cherenkov Counter

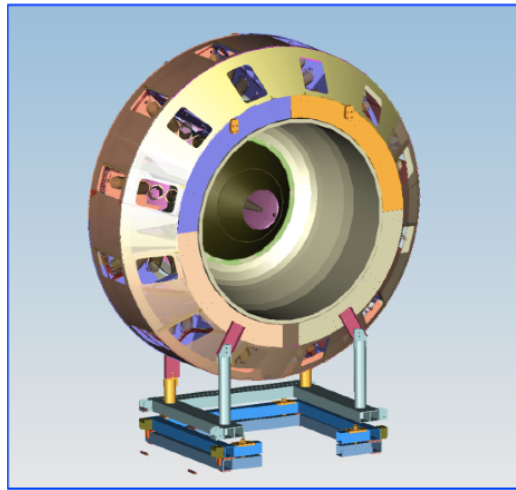


Figure 2.13: The High Threshold Cherenkov Counter detector.

The HTCC will be used to generate fast trigger signal. It will be installed just upstream of the Drift Chambers and shall introduce minimal amount of materials. At the same time the HTCC will provide efficient coverage of the CLAS12 acceptance with no gaps or overlaps. The HTCC is one unit. Its core component is a multifocal mirror consisting of 60 lightweight composite ellipsoidal mirrors. Each sector will be covered with 2 identical half-sector mirrors that are focusing Cherenkov light on eight 5 inch phototubes. The system is required to provide high rejection of charged π meson and low background noise for reliable identification of scattered electrons.

2.2.6 The Low Threshold Cherenkov Counter

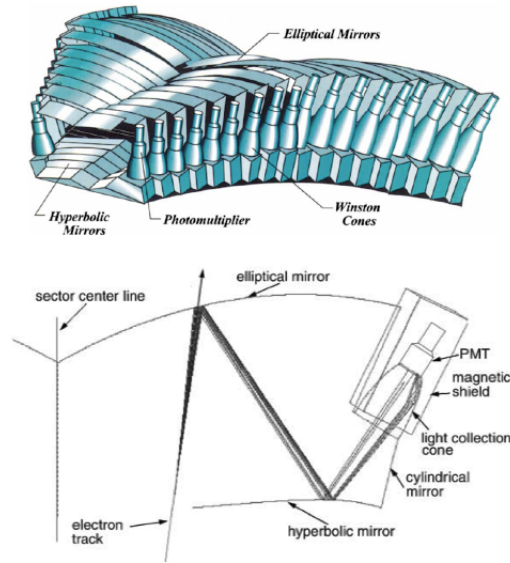


Figure 2.14: The Low Threshold Cherenkov Counter detector.

The LTCC system will be part of the forward detector and will be used for pion identification. The LTCC will consist of six sectors of lightweight mirrors, light collecting cones, 5" PMTs and magnetic shields. The sectors will be filled with C_4F_{10} gas, providing pion identification from 3.5 up to 9 GeV/c. The LTCC is required to have excellent efficiency over the forward angular acceptance.

2.2.7 The Preshower Calorimeter

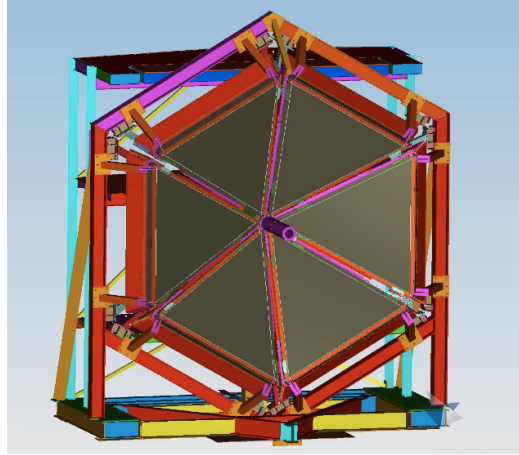


Figure 2.15: The Preshower Calorimeter.

The CLAS12 detector will include the existing electromagnetic calorimeters of the CLAS detector with a pre-shower calorimeter installed in front of it. Calorimeters in CLAS12 will be used mainly for identification of electrons, photons, $\pi^0 \rightarrow \gamma\gamma$ and neutrons. The PCAL, as well as EC, are sampling calorimeters. They consist of six modules. Each PCAL module will have a triangular shape and will be composed of 15 layers. Each layer will be constituted of 1cm thick scintillators, segmented into 4.5cm wide strips, sandwiched between lead sheets of 2.2mm. One layer will correspond to about 5.5 radiation lengths. Scintillator layers will be grouped into three readout views. Each view will have 5 layers. Light read out will be performed using 1mm diameter wavelength shifting fibers inserted into holes along the strips and connected to PMTs in one end.

Chapter 3

The CLAS12 RICH

The Semi Inclusive Deep Inelastic Scattering requires a good separation between pions, kaons and protons. In the basic configuration of the CLAS12 spectrometer, this separation is not well provided in the region between 3 and 8 GeV/c by the baseline detectors. A new detector is therefore required to provide this separation. This is possible using a Ring Imaging Cherenkov with an innovative focusing system.

3.1 The Cherenkov effect

The Cherenkov radiation is electromagnetic radiation emitted by a charged particle traveling in a material faster than the light velocity in that medium. The velocity of light in a material is given by the expression:

$$\beta c = v = c/n, \tag{3.1}$$

where n is the refractive index of the material and c the light velocity in vacuum. A particle emits Cherenkov radiation when it has a velocity $v > c/n$. The Cherenkov effect can be explained in term of classical electromagnetism. A charged particle passing through a dielectric medium polarize the atoms of the material. If the polarization is asymmetric it generates time-varying electric dipole that emits electromagnetic radiation. If the speed of the particle is smaller of the velocity of the light in that medium, his polarization is symmetric. The emitted wave are symmetrically distributed and they interfere destructively. Instead if the speed of the particle is bigger than the

velocity of the light in that medium, the polarization is symmetric respect the azimuthal angle (ϕ) but it is not respect the polar angle (θ), thus creating a coherent wave-front with a specific angle respect to the particle trajectory, called Cherenkov angle θ_{Ch} .

As you can see in Fig. 3.1 the coherent wave-front of the electromagnetic

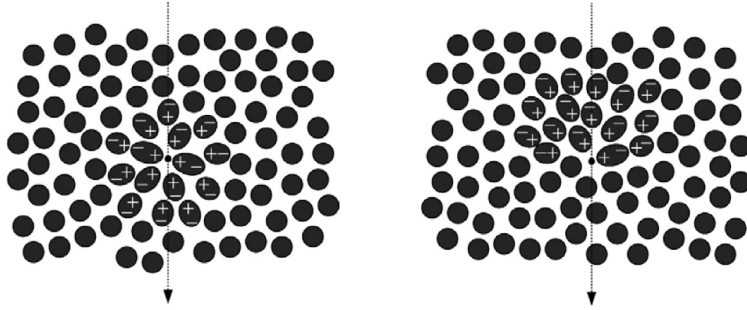


Figure 3.1: The medium polarization for a particle slower (left) and faster (right) than the velocity of the light in that medium.

wave has a conical shape and it is emitted with an angle θ_{Ch} respect the particle trajectory.

In order to have a coherent wave front, the particle has to travel the path AB

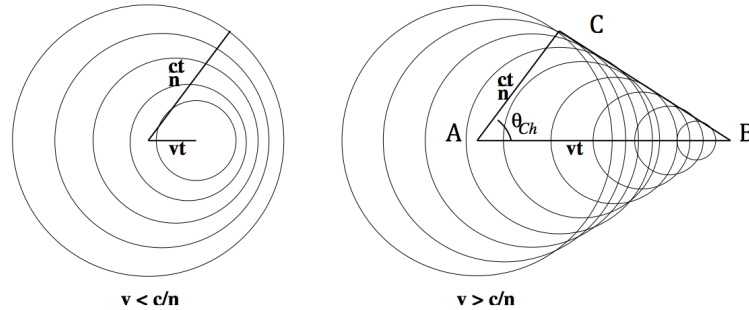


Figure 3.2: The Huygens representation of a particle travelling lower (left) and faster (right) than the speed of the light.

in the same time the light propagates from A to C. In the interval Δt the particle covers a distance $AB = \Delta t \cdot \beta c$ and the light a distance $AC = \Delta t \cdot (c/n)$.

Thus we get the relation:

$$\cos \theta_{Ch} = \frac{AC}{AB} = \frac{\Delta t \cdot (c/n)}{\Delta t \cdot \beta c} = \frac{1}{\beta n}, \quad (3.2)$$

where θ_{Ch} is the Cherenkov angle, n is the refraction index of the medium and $\beta = v/c$. From this relation you can notice that the Cherenkov angle depends only on the velocity of the particle in the material and on the refractive index of the medium. For a given refraction index the Cherenkov angle increases up to a maximum $\theta_{max} = \arccos(1/n)$ for $\beta = 1$. From the relation 3.2 you can realize that the Cherenkov effect is a threshold effect. This means that the effect happen on if the speed of the particle is bigger than the threshold velocity:

$$\frac{1}{\beta n} \leq 1 \Rightarrow \beta = \frac{v}{c} \geq \frac{1}{n} \Rightarrow v_{th} = \frac{c}{n},$$

where v_{th} is the threshold velocity. If we define $\gamma = \frac{1}{\sqrt{1-\beta^2}}$ and $p = m\gamma\beta$, with the rest mass of the particle, and imposing $c=1$, we can compute the threshold momentum:

$$p_{th} = \frac{m}{\sqrt{n^2 - 1}}$$

From this relation you can observe that the momentum threshold is inversely proportional to the refractive index and the threshold velocity reach the limit value of c if n is equal to one. The frequency spectrum of the emitted radiation is from the infrared up to the ultraviolet.

3.2 The number of photons and detections resolution

The energy-loss of one particle due to the Cherenkov effect is much smaller than the energy-loss due to ionization (Bethe-Block). Indeed also if the particle speed tends to the limit value $\beta \rightarrow 1$, the energy-loss for ionization is 100-times bigger than the Cherenkov effect one. This is why scintillators are not employed in Cherenkov detectors.

The number of photons emitted from a charged particle with charge Z in a

material with refraction index n , for unit length and unit of wavelength, is given by the Frank-Tamm relation:

$$\frac{d^2N}{dx d\lambda} = \frac{2\pi Z^2 \alpha}{\lambda^2} \left(1 - \frac{1}{\beta^2 n^2(\lambda)} \right), \quad (3.3)$$

where α is the fine structure constant. If we make the hypothesis of a straight trajectory and integrating along x we can compute the number of photons between λ and $\lambda + d\lambda$:

$$\frac{dN}{d\lambda} = \frac{2\pi LZ^2 \alpha}{\lambda^2} \left(1 - \frac{1}{\beta^2 n^2(\lambda)} \right). \quad (3.4)$$

If we integrate in the given wavelength range the previous expression we obtain the number of photons emitted by a particle on a straight trajectory:

$$N = 2\pi LZ^2 \alpha \int \left(1 - \frac{1}{\beta^2 n^2(\lambda)} \right) \frac{d\lambda}{\lambda^2} = 2\pi LZ^2 \alpha \int \sin^2(\theta_{Ch}(\lambda)) \frac{d\lambda}{\lambda^2}. \quad (3.5)$$

When you compute the number of photons you have to take into account several factors that can determine signal-loss: the transparency T of the material, the reflectivity R of the mirrors, the quantum efficiency Q of the photo-detectors. If we neglect the variation of θ_{Ch} with λ , the number of detected photo-electron is [16]:

$$N_{pe} = N_0 Z^2 L \sin^2(\theta_{Ch}), \quad (3.6)$$

where L is the thickness of the radiator and $N_0 = 2\pi\alpha \int \varepsilon Q T R \frac{d\lambda}{\lambda^2}$ is the quality factor of the detector.

Higher is N_0 (then the number of photo-electron) better is the detector. The identification of the particles is limited by the resolution in the Cherenkov angle measurement. The minimum difference between Cherenkov angles $\Delta\theta_{m_1, m_2}$ necessary to separate two different particles with masses m_1 and m_2 momentum p , with a certain number of sigmas n_σ , is given by the following equation:

$$\Delta\theta_{m_1, m_2} = \frac{m_2^2 - m_1^2}{2n_\sigma} \frac{\sqrt{N_{pe} L_d}}{p^2}. \quad (3.7)$$

where L_d is the total length of the detector. The resolution $\frac{\sigma_\beta}{\beta}$ of the detector depends on the resolution of the Cherenkov angle and from the number of photoelectrons N_{pe} is given by:

$$\frac{\sigma_\beta}{\beta} = \tan(\theta) \frac{\sigma_\theta}{\sqrt{N_{pe}}}. \quad (3.8)$$

3.3 Cherenkov detectors

Two are the fundamental properties used in the Cherenkov detectors: the fact that there is a threshold above which the effect occurs and that the shape of the emitted radiation is a cone with angle θ_{Ch} with respect the particle trajectory. The first property is used in threshold detectors, the second in differential and ring imaging detectors.

3.3.1 The Threshold Cherenkov Detectors

Threshold counters detect particles with a speed higher than the threshold value. For the identification of particles with same momentum but different mass you have to choose a radiator with the appropriate refraction index n . If n is such that:

$$\beta_1 < \frac{1}{n} < \beta_2, \quad (3.9)$$

where β_1 is the speed of the heavier particle and β_2 is the speed of the lighter particle, only the second one produces Cherenkov radiation. Thus one can distinguish the 2 particles. The problem of these kind of detectors is that you have to work in the neighborhood of θ_{Ch} , thus with small angles and small number of photons.

3.3.2 The Differential Cherenkov Detectors

Differential Cherenkov detectors reveal only particles with a speed included in the range $\Delta\beta$ defined from the geometry of the detector, since β is linked to the angle θ_{Ch} by the relation 3.2. All the particles with speed $\beta > 1/n = \beta_{min}$

are above threshold. The Cherenkov angle increase with β up to the maximum reflection angle θ_r . In correspondence on θ_r photons are not detected. We can compute the maximum reflection angle from the Snell's law $\sin \theta_r = 1/n$. Thus you can obtain the maximum beta:

$$\beta_{max} = \frac{1}{\sqrt{n^2 - 1}}. \quad (3.10)$$

The maximum precision you can achieve is $\frac{\Delta\beta}{\beta} = 10^{-6}$.

3.3.3 The Ring Imaging CHerenkov

Ring Imaging CHerenkov are particular detectors that measure the Cherenkov angle. The image of the conic wavefront projected on a surface perpendicular to particle trajectory is a ring. The radius of this ring depend on the particle velocity. There are two main working scheme for a RICH. If a RICH detector collects the light directly on the photodetector region, without changing the path of the photons, is working in the proximity (or direct light) scheme (Figure 3.3).

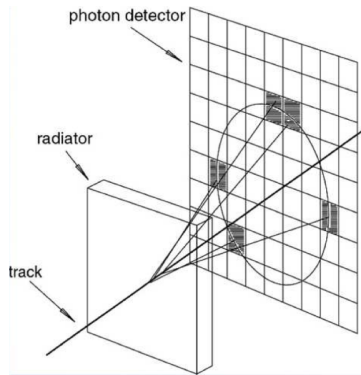


Figure 3.3: Scheme of the principle of a RICH detector working in proximity mode.

If the path of the photons is changed with a focusing mirror the RICH is working in the so-called focusing(or reflected) scheme (Figure 3.4).

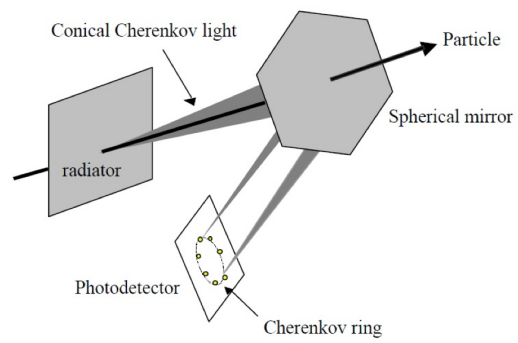


Figure 3.4: Scheme of the principle of a RICH detector with spherical focusing mirrors.

3.4 The CLAS12 RICH

The CLAS12 baseline detectors don't provide a well separation between pions, kaons, and protons in the region between 3 and 8 GeV/c. This can be provided by a RICH detector. The goal of this system is the identification of pions, kaons and protons from 3 up to 8 GeV/c, with a pion rejection factor $\approx 1:500$ and a corresponding $4\text{-}\sigma$ pion-kaon separation. This rejection factor is required because the number of pions is about ten times larger than the kaons one. The working region of the RICH detector is shown in Fig. 3.5 in comparison with the FTOF system. Many constraints are imposed

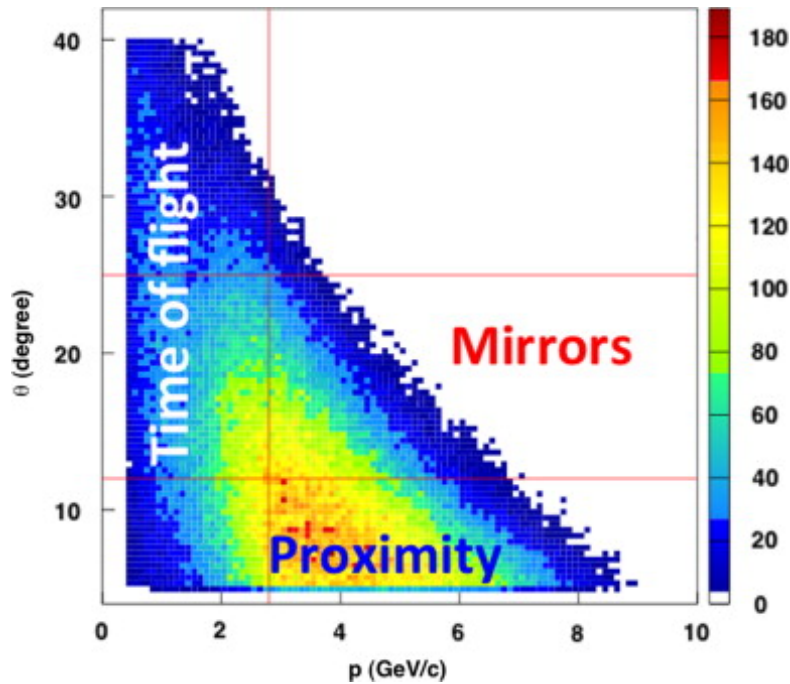


Figure 3.5: Scattering angle versus momentum of the hadrons in the CLAS12 forward spectrometer. The FTOF counter covers the low momentum region; a RICH is suitable for the high momentum region.

upon the RICH design by the presence of other detectors of CLAS12 that are already in the construction phase. To fit into the CLAS12 geometry, the RICH should have a six-sector projective geometry occupying the space between the torus cryostats and therefore covering the scattering angles from

5° to 30° . The available space for the RICH module is basically the same as that for one LTCC sector. The external frame has a trapezoidal shape,

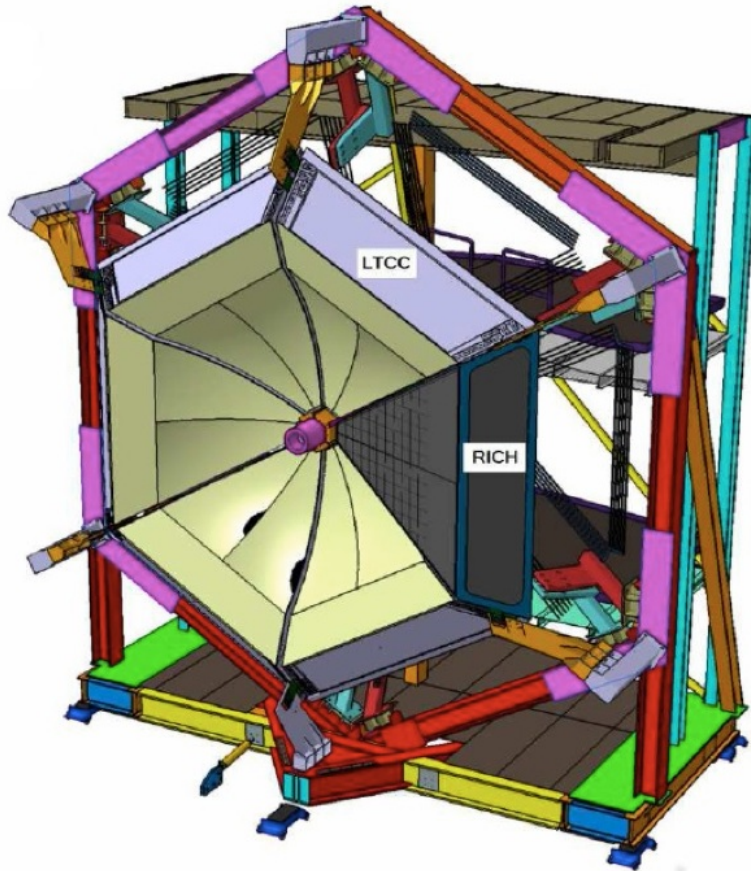


Figure 3.6: The CLAS12 spectrometer with one RICH module replacing one of the LTCC modules.

with a major base of about 4.3 meters, a height of about 3.8 meters and a depth of about 1 meter and it is tilted by 65° with respect to the beam axis. A schematic view of the RICH sector within the CLAS12 spectrometer is shown in Fig. 3.6. The RICH design incorporates aerogel radiators, visible light photon detectors, and a focusing mirror system which will be used to reduce the photon detectors area to 1 m^2 .

The CLAS12 RICH is a double configuration detector. It will work both in

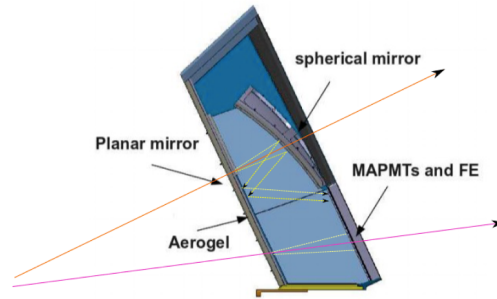


Figure 3.7: Schematic lateral view of a RICH sector.

proximity and focusing scheme. The proximity system will be used for the forward scattered particles ($\theta < 13^\circ$). Particles with momenta 3 - 8 GeV/c will travel through 2 cm aerogel tiles and their emitted Cherenkov light will be directly detected (as you can see in Figure 3.8). For larger incident particle

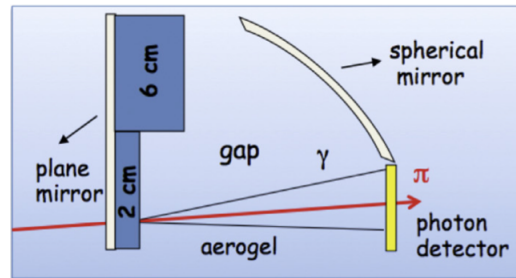


Figure 3.8: The RICH proximity scheme.

angles ($13^\circ < \theta < 35^\circ$) a focusing scheme will be used. In this case particles will have momenta of 3 - 6 GeV/c. As shown in Figure 3.9, the Cherenkov light will be produced by a thicker aerogel (6 cm), focused by a spherical mirror, undergo two further passes through the thin radiator material and a reflection from planar mirrors before detection.

3.4.1 The Aerogel Radiator

Silica aerogel, with a refractive index of $n = 1.05$, has been chosen as the radiator material for the CLAS12 Ring Imaging Cherenkov detector. Silica aerogel is an amorphous solid network of SiO₂ nano-crystals with an

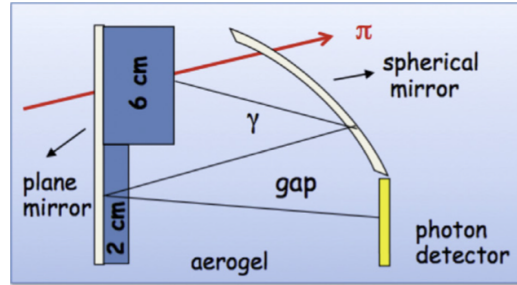


Figure 3.9: The RICH focusing scheme.

extremely low macroscopic density and a refractive index close to 1. The performance of the detector is closely related to the optical properties of the aerogel: any angular dispersion of the emitted photons affects the precision of the Cherenkov angle measurement. The chromatic dispersion (the variation of the refractive index as function of the wavelength) was studied during the test beam at CERN [11] [12]. The dependence of the refractive index on the wavelength is approximately given by the dispersion relation [13]:

$$n^2(\lambda) - 1 = \frac{P_1 \lambda^2}{\lambda^2 - P_2^2}; \quad (3.11)$$

where P_1 and P_2 are parameters depending on the material characteristics. These parameters are obtained by fitting the measured distribution, as shown in Fig. 3.10. In Fig. 3.11 is shown a study of the transmittance of different tiles, where it is possible to notice that the the transmittance is above 50% in the wavelength range where the quantum efficiency of the PMTs is greater (300 - 500 nm). An issue in the use of tiles of aerogel is the refraction through the aerogel surface. This aspect, that is critical in the focusing mode due to multiple passage through the radiator, will be analyzed in more detail Chapter 5.

3.4.2 The Photon Detectors

There are several requirements determining the choice of the photon detectors. They must provide a spatial resolution of less than 1cm^2 , with minimal dead-space and a good response in the visible region, that is the region of

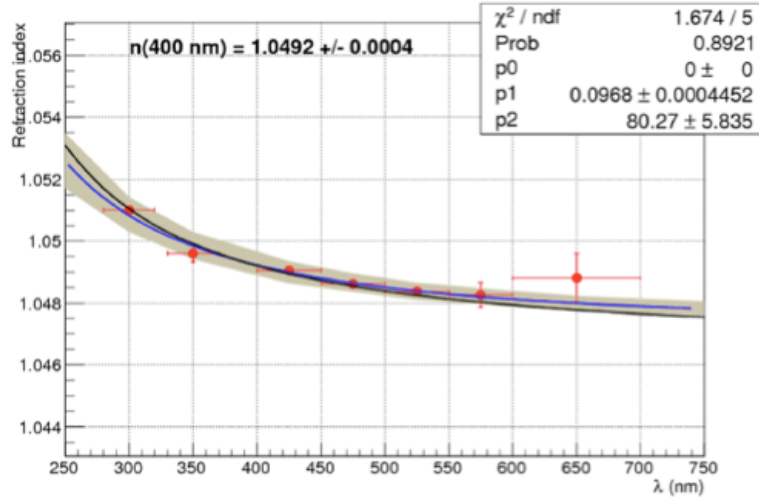


Figure 3.10: Measured refraction index as a function of the wavelength for an aerogel tile with $n = 1.05$ nominal refractive index and $t = 2$ cm aerogel. The blue curve is a fit of the data using the dispersion law (the error is indicated by the gray band).

interest by combining the emission of the Cherenkov light spectrum and the transmittance of the aerogel radiator. The H8500 MultiAnode PhotoMultiplier Tubes (MAPMTs) by the Hamamatsu company is an adequate compromise between detector performance and costs [14]. Each tube has a matrix of 8×8 pixels of 6×6 mm² size and these tubes are also sufficiently insensitive to the residual magnetic field expected in the RICH position. The H8500 PMTs are not recommended by the firm for the detection of single photons, however our study has shown that they are able to measure single photons with a sufficient efficiency for a RICH detector. By illuminating the center of each pixel of a MAMPMTs with a low emitting blue laser light, inside a black box in order to isolate the photo multiplier from any background light, and measuring the charge spectra with an ADC, it is possible to detect clearly the single photon peak as shown in Fig. 3.13. The photoelectron peak is well separated from the pedestal; therefore, it is possible to put a cut above the pedestal without losing a significant part of the signal and distinguish the photon contribution. This demonstrates that the H8500 PMTs are suitable detectors for a single photon measurement.

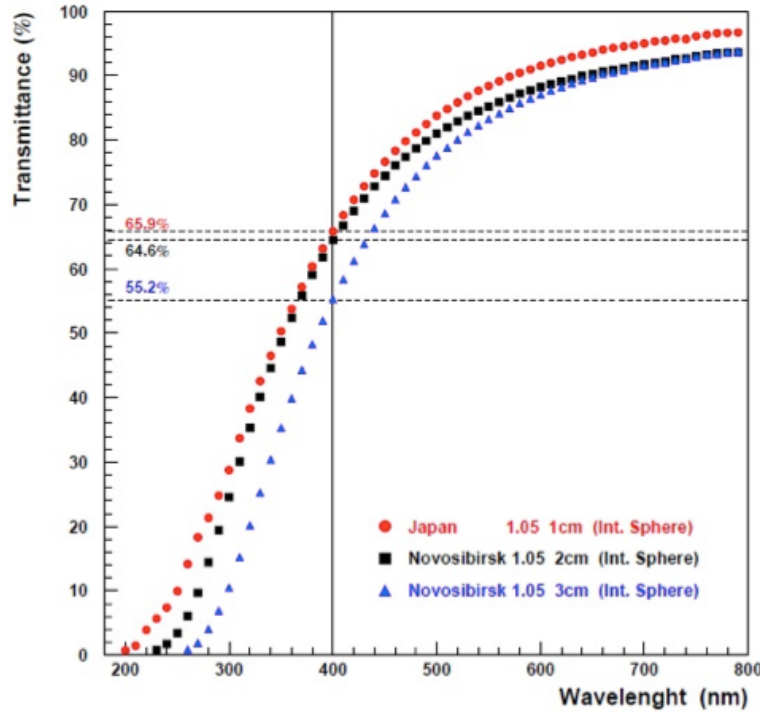


Figure 3.11: Comparison of the transmittance measured as a function of the wavelength for a 1cm Matsushita tile (red) and a 2cm and 3cm Novosibirsk tiles (black and blue). All tiles have nominal refractive index $n = 1.05$.

3.4.3 The Focusing System

The CLAS12 RICH detector exploits an elaborated mirror focusing system in order to contain the Cherenkov photons within the module and direct them toward the photodetectors. Photons produced at large angles (i.e. in the 6 cm thick tiles of aerogel) are reflected and focused to the MAPMT region by two large mirrors (several square meters), a spherical mirror placed above the MAPMT array and a planar one just before the aerogel tiles. In addition to the two main mirrors, the inner walls on the sides of the module structure will also be covered by mirrors, in order to keep all the produced Cherenkov photons within the RICH module. Beyond reflectivity, that is needed higher than 90% in the visible and near UV wavelength regions, two

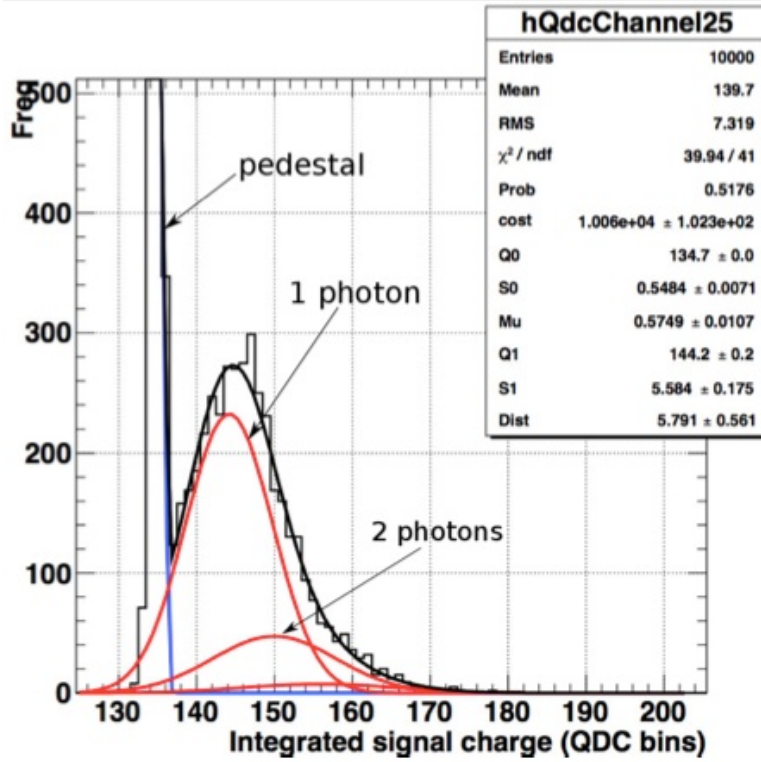


Figure 3.12: Integrated signal charge spectrum for one pixel of the H8500 MAPMT when illuminated with laser light ($\lambda = 407.2\text{nm}$) and for an MAPMT high voltage of -1075V .

important parameters for the design and the construction of these mirrors are: the rigidity, that should be high to ensure that, during several years of operation, deviations from the nominal position do not affect the RICH performances, and the material budget that should be kept as low as possible in order to preserve the performances of the detectors placed just behind the RICH.

Spherical Mirror

The curved mirror covers a surface of about 3.5 m^2 and is tilted by 65° with respect the beam axis. The challenge in manufacturing this mirror is due to its size, because such large areas cannot be coated with the reflecting material

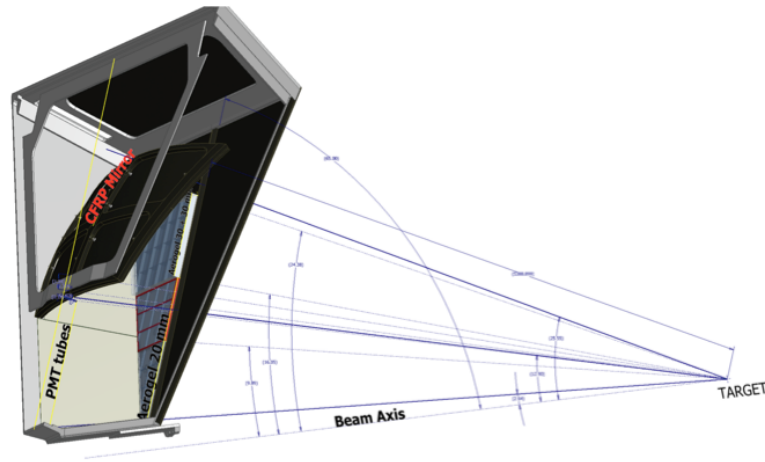


Figure 3.13: A 3D view of the CLAS12 RICH.

in a single-step process. This imposes the choice of dividing the mirrors into smaller sub-mirrors with a surface of about 1 m^2 . The four mirrors will be mounted on a common frame and can be individually adjusted in angle and position by means of three different jacks. The optimal radius of curvature has been studied in Monte Carlo simulations [15]. It was seen that the best particles separation is achieved using a radius of curvature of 4000 mm. The total material budget needs to be as small as possible, without impacting the stiffness and the durability of the structure. A well assessed method to fit all the above characteristics is to use a Carbon-Fiber Reinforced Polymer (CFRP) structure, sandwiching a light core material, coated with a reflective material. A mirror demonstrator, with a core made of 25 mm core of rohacell foam, has been tested under different humidity condition. The results will be shown in Chapter 6.

Planar Mirror

The planar mirror is placed on the entrance side of the module and has a surface area of approximately 3.5 m^2 . It works also as a support for the radiator and sends back the light focused by the spherical mirror. It will be segmented into six smaller sub-mirrors made of two thin (0.8 mm) glass skins and with an aluminum honeycomb core. These sub-mirrors will be mounted

on a CFRP support that will also constitute the entrance window of the RICH module.

Chapter 4

Single Photon Resolution

The single photon resolution is the key point for a good particle separation in a RICH detector. There are several factors contributing to it:

- the emission point ($\sigma_{\theta_{Ch}}^{emission}$);
- the chromatic aberrations of the radiator ($\sigma_{\theta_{Ch}}^{ch}$);
- the readout accuracy ($\sigma_{\theta_{Ch}}^{pixel}$);
- the error induced by the focusing system ($\sigma_{\theta_{Ch}}^{focus}$).

Each one contributes to the Cherenkov angle resolution by:

$$\sigma_{\theta_{Ch}}^{tot} = \sqrt{\sum_i (\sigma_{\theta_{Ch}}^i)^2}. \quad (4.1)$$

Since CLAS12 RICH has an hybrid geometry, for each contribution of eq. 4.1, we have two different values, one resolution value associated to the proximity mode and the another one associated to the focusing mode.

4.1 Emission Point Contribution

The emission point is an error due to the continuous emission of photons along the thickness of the radiator. From geometrical considerations, and

assuming the same emission probability inside the radiator, it is possible to estimate this contribution as:

$$\sigma_{\theta_{Ch}}^{emission} = \frac{d_a \cdot \sin \theta_{Ch} \cdot \cos \theta_{Ch}}{L\sqrt{12}}. \quad (4.2)$$

For $\beta=1$ (maximum θ_{Ch}), $L = 1$ m and $d_a = 2$ cm in the proximity region and $L = 3$ m and $d_a = 6$ cm in the focusing region, the contribution is:

$$\sigma_{\theta_{Ch}}^{emission} = 1.7 \text{ mrad.}$$

4.2 Chromatic Aberrations

The chromatic aberrations contribution takes into account the dispersion of refractive index as a function of λ , which causes a smearing of the Cherenkov angles. Using the measured variation for $n(\lambda)$ shown in Fig. 3.10, it is possible to correlate the measured $\frac{\Delta n}{n}$ to the variation of the Cherenkov angle following the eq. 3.2. In the proximity region, the estimated contribution is: $\sigma_{\theta_{Ch}}^{ch} = 3.3$ mrad. In the focusing region, the estimated contribution is: $\sigma_{\theta_{Ch}}^{ch} = 2.5$ mrad. In this case the double passage through the aerogel reduce the range of observable wavelength.

4.3 Readout Accuracy

The readout accuracy is an error due to the finite granularity of the photodetectors and it contributes to the Cherenkov angle resolution by:

$$\sigma_{\theta_{Ch}}^{pixel} = \arctan \left(\frac{a\sqrt{2}}{L\sqrt{12}} \right) \quad (4.3)$$

where $a = 6$ mm is the pixel size of the photo-detector. In the focusing region ($L = 3$ m) there is an error of:

$$\sigma_{\theta_{Ch}}^{pixel} = 0.82 \text{ mrad.} \quad (4.4)$$

In the proximity region ($L = 1$ m) there is an error of:

$$\sigma_{\theta_{Ch}}^{pixel} = 2.45 \text{ mrad.}$$

4.4 Focusing System Resolution

Considering the contributions explained in the previous sections, the total error in the proximity region is $\sigma_{\theta_{Ch}}^{tot} = 4.45$ mrad, while the error in the focusing region is $\sigma_{\theta_{Ch}}^{tot} = 3.1$ mrad. For the focusing system it is required a contribution equal to one third of $\sigma_{\theta_{Ch}}^{tot}$ in order to be considered negligible. Therefore:

$$\sigma_{\theta_{Ch}}^{focus} < 1 \text{ mrad.} \quad (4.5)$$

The focusing system contribution can be written as:

$$\sigma_{\theta_{Ch}}^{focus} = \sqrt{\left(\sigma_{\theta_{Ch}}^{spherical}\right)^2 + \left(\sigma_{\theta_{Ch}}^{aerogel}\right)^2 + \left(\sigma_{\theta_{Ch}}^{planar}\right)^2} \quad (4.6)$$

where $\sigma_{\theta_{Ch}}^{spherical}$ is the spherical mirror contribution, $\sigma_{\theta_{Ch}}^{planar}$ is the planar mirror contribution and $\sigma_{\theta_{Ch}}^{aerogel}$ is the contribution of the aerogel radiator. In section 4.5 and 4.6 will be presented the mirror and aerogel $\sigma_{\theta_{Ch}}$ contribution, respectively, and in particular the correlation with surface imperfection.

4.5 Mirror $\sigma_{\theta_{Ch}}$ contribution

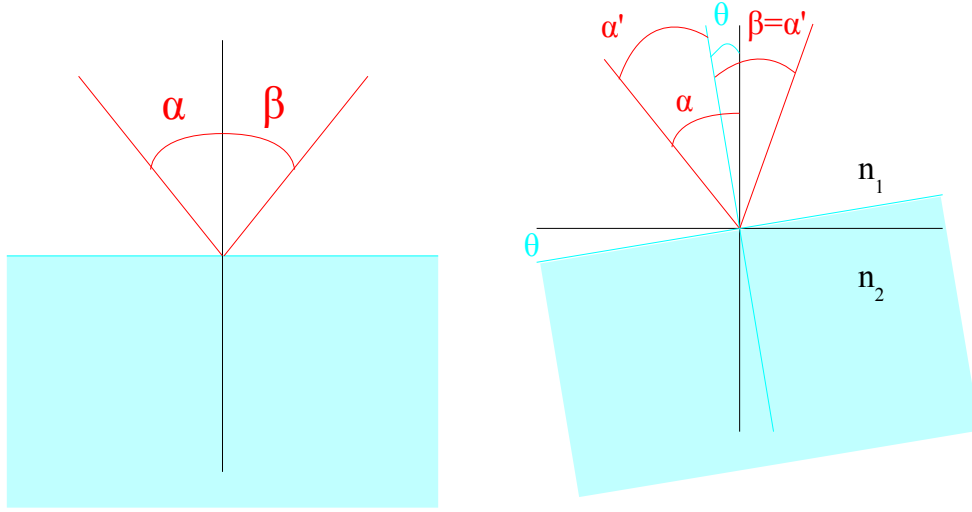


Figure 4.1: Reflection on an ideal (left) and real (right) surface.

In Fig. 4.1 is shown the reflection of light ray from a smooth surface. Incident and reflected angle are the same:

$$\alpha = \beta. \quad (4.7)$$

Considering a surface imperfection, i.e. the normal to the surface has an angular error θ_{mir} with respect the nominal direction (Fig. 4.1), the reflection angle β of equation 4.7 become:

$$\beta = \alpha' = \alpha - 2\theta_{mir}. \quad (4.8)$$

The expression of the light angular dispersion (after one reflection) is therefore:

$$\sigma_{\theta_{light}} \sim 2 \cdot \sigma_{\theta_{mir}}. \quad (4.9)$$

To calculate the two contributions $\sigma_{\theta_{Ch}}^{planar}$ and $\sigma_{\theta_{Ch}}^{spherical}$ is necessary to rescale $\sigma_{\theta_{light}}$. That means divide the path after the reflection (2 m for the spherical

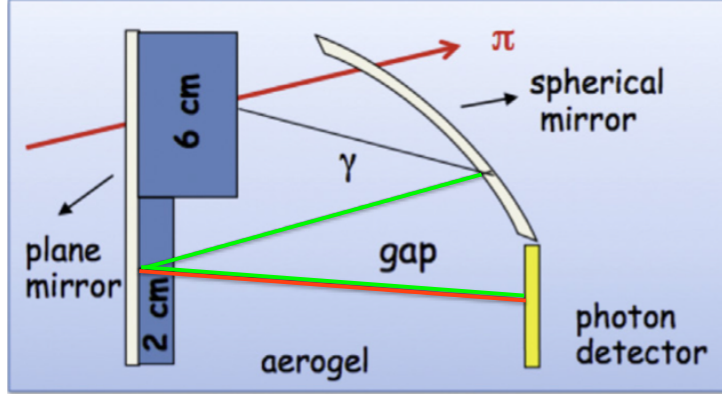


Figure 4.2: In green the 2 m path after the spherical mirror reflection.
In red the 1 m path after the planar mirror reflection.

mirror, 1 m for the planar one, see Fig. 4.2) for the total path of the photons. Therefore the contribution of the planar mirror is:

$$\sigma_{\theta_{Ch}}^{planar} = \sigma_{\theta_{light}} \cdot \frac{1 \text{ m}}{3 \text{ m}} = 2 \cdot \sigma_{\theta_{mir}} \cdot \frac{1}{3} = \frac{2}{3} \sigma_{\theta_{mir}}, \quad (4.10)$$

and that of the spherical mirror is:

$$\sigma_{\theta_{Ch}}^{spherical} = \sigma_{\theta_{light}} \cdot \frac{2 \text{ m}}{3 \text{ m}} = 2 \cdot \sigma_{\theta_{mir}} \cdot \frac{2}{3} = \frac{4}{3} \sigma_{\theta_{mir}} \quad (4.11)$$

4.6 Aerogel $\sigma_{\theta_{Ch}}$ contribution

In all the following calculation we assume $n_1 = 1$ (air) and $n_2 = 1.05$ (aerogel). The refraction of light rays through the interface of two materials with

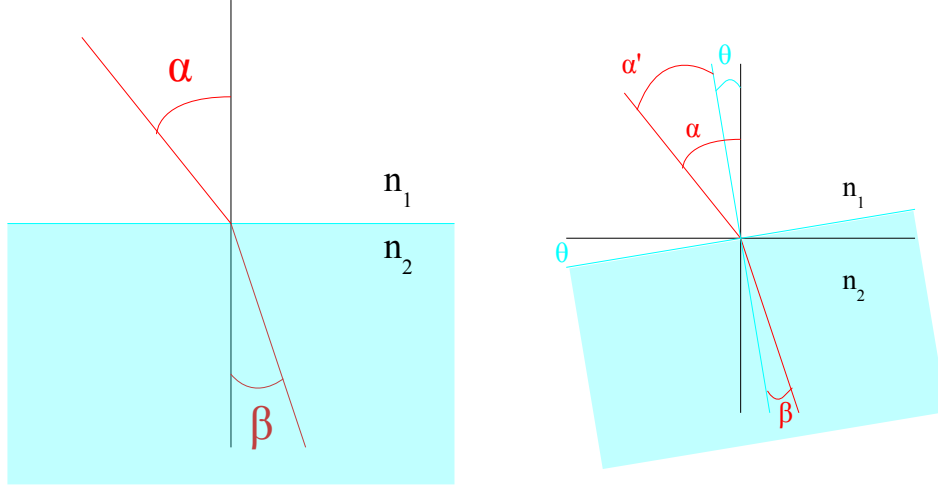


Figure 4.3: Reflection on a real material.

different refractive index is governed by Snell's Law:

$$n_1 \sin \alpha = n_2 \sin \beta \quad (4.12)$$

where n_1 and n_2 are the refractive indices of the first and second material, respectively, and α and β are the angles of the two light rays respect the normal to the surface (see Fig. 4.3).

The angle β is

$$\beta = \arcsin \left(\frac{n_1}{n_2} \sin \alpha \right). \quad (4.13)$$

The refraction angle β given by Snell's law in case of a surface imperfection (small angular shift θ_{aer} , see Fig. 4.3) is:

$$\beta = \theta_{aer} + \arcsin \left(\frac{1}{n} \sin \alpha' \right) = \theta_{aer} + \arcsin \left(\frac{1}{n} \sin(\alpha - \theta_{aer}) \right) \quad (4.14)$$

The angular dispersion of the transmitted photons due the aerogel surface imperfections θ_{aer} , at a given incident angle α , can be approximated as:

$$\sigma_{\theta_{light}} \sim \sigma_{\theta_{aer}} + \left(\frac{1}{n} \sin(\alpha - \sigma_{\theta_{aer}}) \right) \sim \left(1 - \frac{1}{n} \right) \sigma_{\theta_{aer}} \sim 0.05 \sigma_{\theta_{aer}}. \quad (4.15)$$

Up to now it has been considered only one surface. In case of transmission

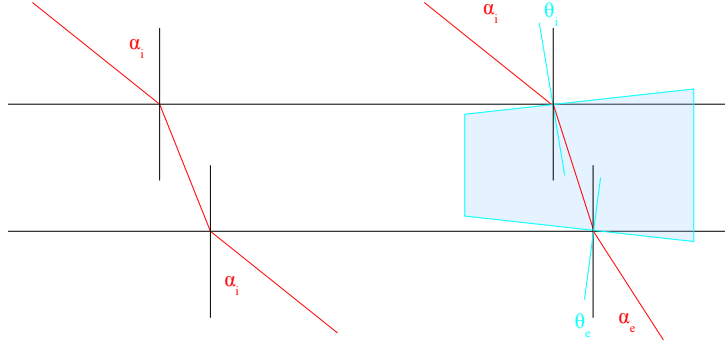


Figure 4.4: Left: in the ideal case $\alpha_e = \alpha_i$. Right: in the real case $\alpha_e \neq \alpha_i$.

through a material with refractive index n (e.g. an aerogel tile) light rays are refracted twice. In the ideal case (material with parallel surfaces, Fig. 4.4) the beam light is only shifted. Instead if there are imperfection on both faces the exit angle is:

$$\begin{aligned} \alpha_e &= \theta_e + \arcsin(n \sin(\beta - \theta_e)) = \\ &= \theta_e + \arcsin\left[n \sin\left(\theta_i - \theta_e + \arcsin\left[\frac{1}{n} \sin(\alpha_i - \theta_i)\right]\right)\right] \end{aligned} \quad (4.16)$$

where α_i is the angle on the incoming ray, α_e is the outgoing beam angle and θ_i and θ_e are the small angular errors of the two aerogel surfaces. In the small angle approximation:

$$\alpha_e \sim \alpha_i + (n - 1)(\theta_i - \theta_e)$$

and (making the hypothesis of no correlation between θ_i and θ_e) the angular dispersion of the light is

$$\sigma_{\theta_{light}} = (n - 1)\sqrt{\sigma_{\theta_i}^2 + \sigma_{\theta_e}^2} \sim 0.05 \cdot \sqrt{2} \cdot \sigma_{\theta_{aer}}. \quad (4.17)$$

Using eq. 4.16 and eq. 4.17 it possible to compute the dispersion of light

beam that pass twice through an aerogel tile (as will happen in the RICH focusing configuration):

$$\sigma_{\theta_{light}} = (n - 1) \sqrt{\sigma_{\theta_i}^2 + \sigma_{\theta_e}^2 + \sigma_{\theta_i}^2 + \sigma_{\theta_e}^2} \sim 0.05 \cdot 2 \cdot \sigma_{\theta_{aer}} \sim 0.1 \cdot \sigma_{\theta_{aer}}. \quad (4.18)$$

Also in this case it is necessary to rescale $\sigma_{\theta_{light}}$ for the calculation of $\sigma_{\theta_{Ch}}^{aerogel}$ contribution. The total path of the Cherenkov photons is 3 m, the partial path after aerogel refraction is 1 m. Therefore the aerogel contribution is:

$$\sigma_{\theta_{Ch}} = \sigma_{\theta_{light}} \cdot \frac{1 \text{ m}}{3 \text{ m}} = 0.1 \cdot \sigma_{\theta_{aer}} \cdot \frac{1}{3} = 0.03 \sigma_{\theta_{aer}}. \quad (4.19)$$

Chapter 5

Aerogel Characterization Measurement

The performance of a RICH detector is closely related to the optical properties of the aerogel radiator. Any angular dispersion of the emitted photons affects the precision of the Cherenkov angle measurement. The refractive index uniformity is generally a key property of a good Cherenkov radiator. However there are also others parameters that can affect the angular distribution of the produced photons, like surface irregularities and thickness variations. Generally speaking the measured aerogel properties result usually worse than the simulated ones. In the literature this fact is attributed to a generic forward scattering effect whose origin is not well understood (see [6] and [7]).

The aim of the thesis work has been to develop a not-invasive measurement protocol to study in detail the relevant aerogel properties. The Japanese BTR 12-3a aerogel tile was used as sample test in all the measurements, being hydrophobic (not sensitive to the ambient humidity). With an X-ray radiographic technique we tested the density uniformity of various aerogel tiles. Since the refractive index is related to the density as $n^2 = 1 + \alpha\rho$, with $\alpha = 0.438$, this allows to test also the refractive index uniformity [8] [9]. In order to see the surface imperfections of the aerogel and to measure the local thickness and possible shape deformations ($\sigma_{\theta aer}$), two different measurements were performed. In the first case a 5 axis touching machine was used to measure the height variation on a grid of points along the two faces of the

aerogel tile. This technique provides all the information mentioned before with high precision, but is invasive as the measuring rod touch the aerogel surface at each measured point. It was used to validate the second, not invasive technique. In the second case we sent a laser beam into the aerogel and we measured how the reflected spot position changes moving along the aerogel surface. With the laser setup we didn't measure directly the surface position of the aerogel but his gradient, then with a reconstruction software we have been able to reproduce the surface. As a consequence, with the laser setup it's not possible to measure the absolute thickness of the tile but only the relative variation. However the laser set-up, being compact, movable and relatively inexpensive, offers a not invasive and pretty flexible analyzing tool.

5.1 Touching Machine Measurement



Figure 5.1: The touching machine.

At the end of October 2014 we measured the surface of the aerogel. We used a 3 axis touching machine with 2 more degree of freedom (rotations) for the sensor. The apparatus uses an unique reference frame for both faces. An X marker was printed on one corner of the tile with the purpose of keep trace of the aerogel orientation during the various measurements. We put the origin on the marked side of the tile, on the corner opposite respect the marker (see Figure 5.2).

For each face we recorded 810 points. The machine rod touches the aerogel and calculate the coordinate of the touched point respect the previous defined reference frame. The measured points define a grid of 30 times 27 spatial position. The distance between two adjacent points is 3 mm. The reference frame of the graphs has been changed respect the touching machine one. The coordinates along the surface has been assigned to XY-plane and the aerogel height variation to the zed axis. The origin of this new reference frame is in the bottom-left corner of the front side of the aerogel (see Figure 5.3). Hereinafter the aerogel side with the marker on the right will be called Face₁, the other Face₂.

The reference frame transformations are:

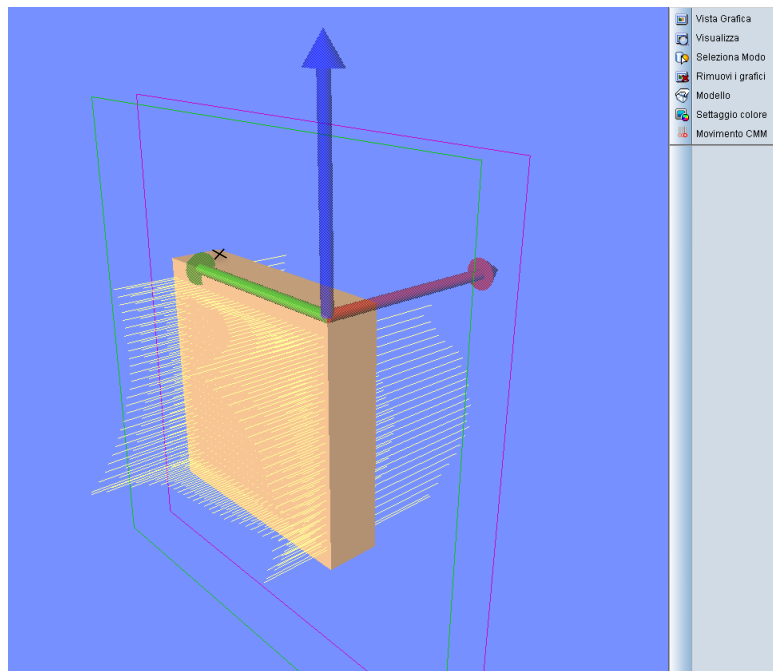


Figure 5.2: The coordinate system of the measurements.
The x axis is red, the y axis is green and the z axis is blu.

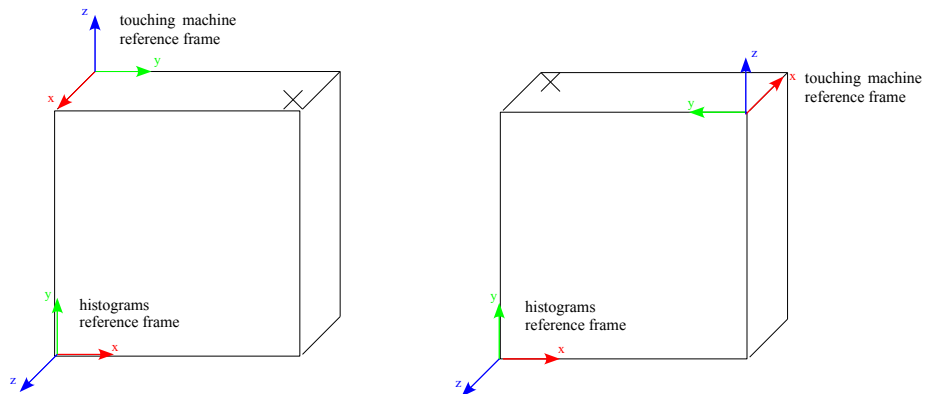


Figure 5.3: The histograms' coordinate system of the 2 Faces.
The black X indicates the marker on the aerogel tile defining Face₁ (left) and Face₂ (right).

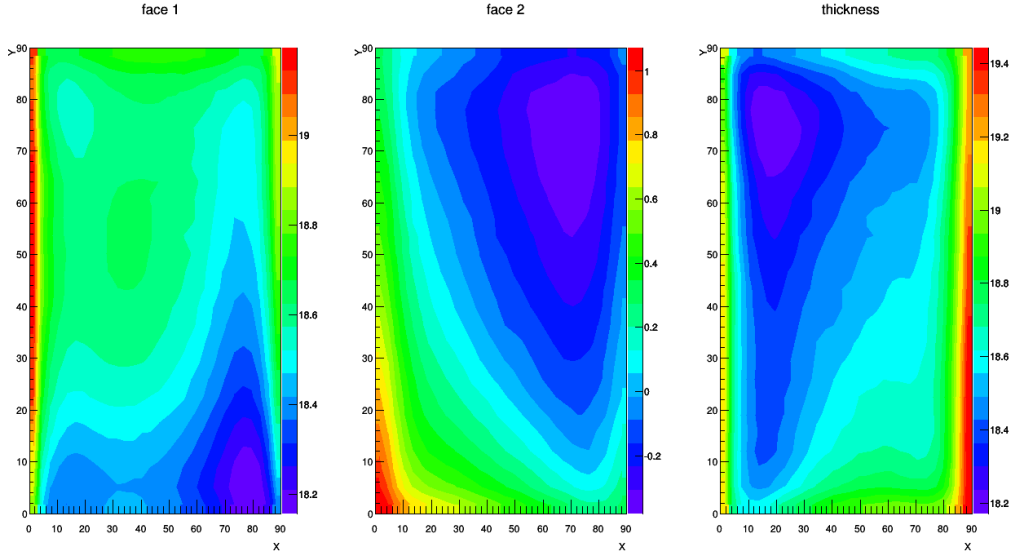


Figure 5.4: The two surface shapes and the thickness of the aerogel sample.

$$\begin{array}{cc}
 \text{Face}_1 & \text{Face}_2 \\
 x_h = \frac{y_{tm}}{3} + 1 & x_h = \frac{90 - y_{tm}}{3} + 1 \\
 y_h = \frac{90 + z_{tm}}{3} - 1 & y_h = \frac{90 + z_{tm}}{3} - 1 \\
 z_h = x_{tm} & z_h = -x_{tm}
 \end{array}$$

where x_h, y_h and z_h are the coordinate used in the histograms and x_{tm}, y_{tm} and z_{tm} are the coordinate used by the touching machine. In Figure 5.4 the results for the two faces and the thickness of aerogel are shown. From this data the gradients ∇_x and ∇_y has been calculated taking the difference between two adjacent points and then dividing by the step between them. The results are shown in Fig. 5.5.

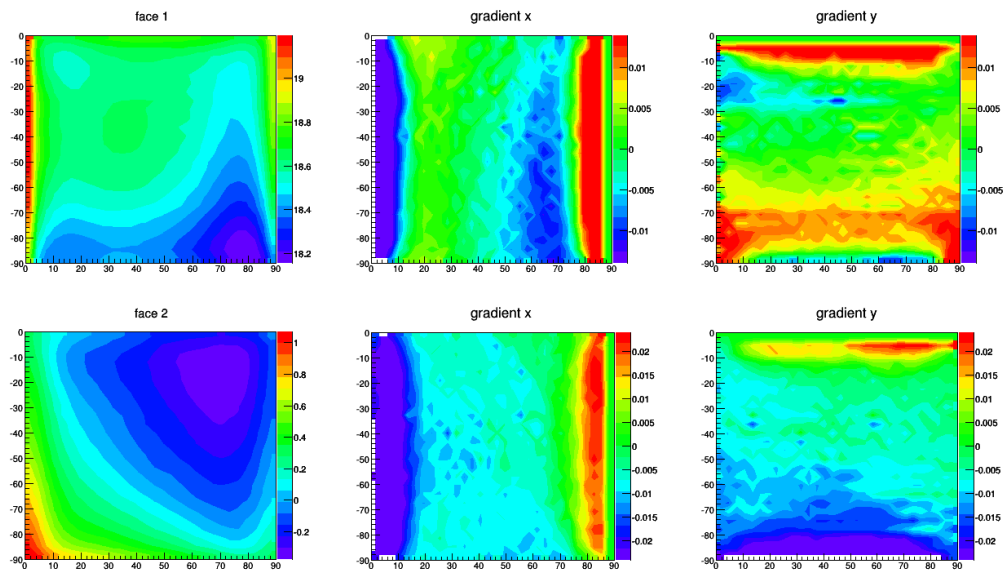


Figure 5.5: Surface gradients ∇_x and ∇_y calculated from the touching machine measurements.

5.2 Laser Reflection Measurement

The laser reflection measurements on the aerogel was done on January 2015. The laser light was sent to the aerogel and then, after having been reflected from the aerogel, on a screen attached to the laser tube. With a CCD camera we took a picture of the spots on the screen. See picture 5.6 for more details. We used an helium-neon laser with 5 mW of power at 632.8 nm. The aerogel

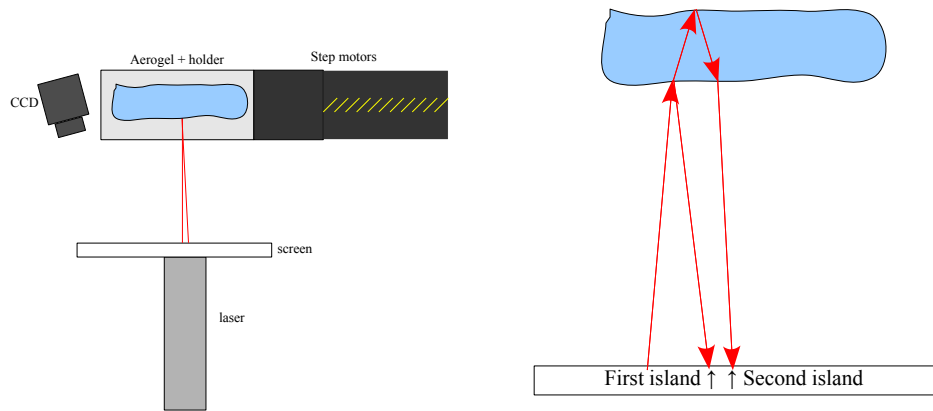


Figure 5.6: The top view of laser reflection measurements scheme (left) and of the double reflection representation (right).

was kept by an holder mounted on two step motors for the movements in the XY-plane. The pictures was done with a CCD camera with 1280x1024 pixels.

As shown in Fig. 5.6 the CCD camera is not exactly in front of screen, so in all the measurements there is a small parallax effect that at this stage was neglected. Pictures of the CCD camera were saved as .txt images. This has made it easier the conversion into a ROOT histogram with a BASH script. In order to measure the gradients ∇_x and ∇_y of the aerogel surface, the first operation was to remove the laser beam source from the pictures. Then with a specially developed software we stored the two remaining spots (hereinafter named reflections) in two different histograms. We defined first (second) reflection the spot with the higher (lower) ADC value (see Fig. 5.7). Finally all the relevant reflection quantities (spot integral, maximum

position, RMS, ...) were stored in a ROOT tree. Looking at the distribution

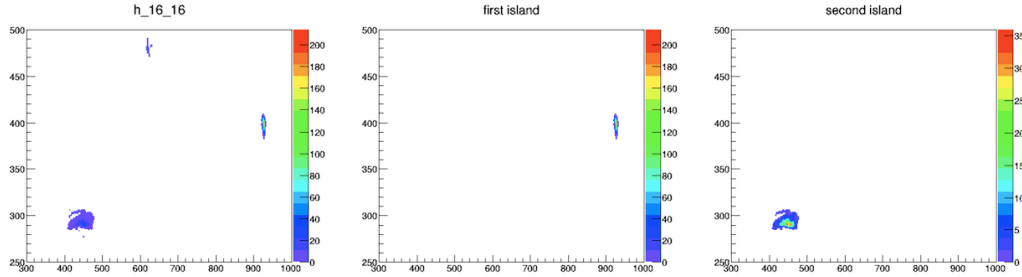


Figure 5.7: The original histogram (with laser source, first and second reflection) and the ones with only the selected first and second reflection, respectively.

of the integral of the two reflected spots (Fig. 5.8 and 5.9) we neglect the measurements with an integral smaller than 500 ADC values corresponding to the cases where the reflected light is outside the screen or is diffused due to a aerogel surface imperfection (scratch). Then we looked to a quantitative way for assigning the measured spots to the first or the second reflection.

The integral and the position of the maximum of the two reflections have

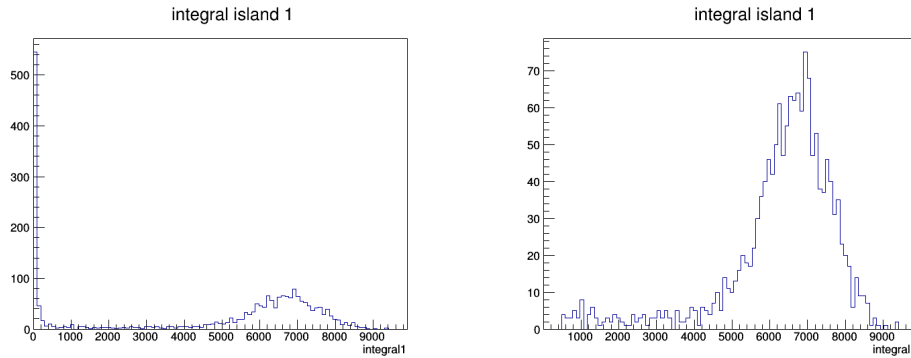


Figure 5.8: The distribution of the integral of the first island before (left) and after (right) the cut.

been compared (see Fig. 5.10) but in the end we found that the best quantity to identify the reflections was the RMS of the spot, defined as the sum in quadrature of the two RMS of the spot projections in X and Y , since it is a

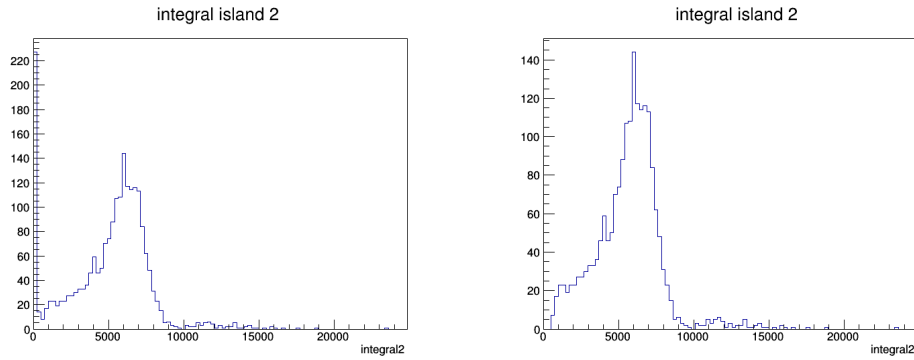


Figure 5.9: The distribution of the integral of the second island before (left) and after (right) the cut.

much less fluctuating quantity respect the other two (Fig. 5.11).

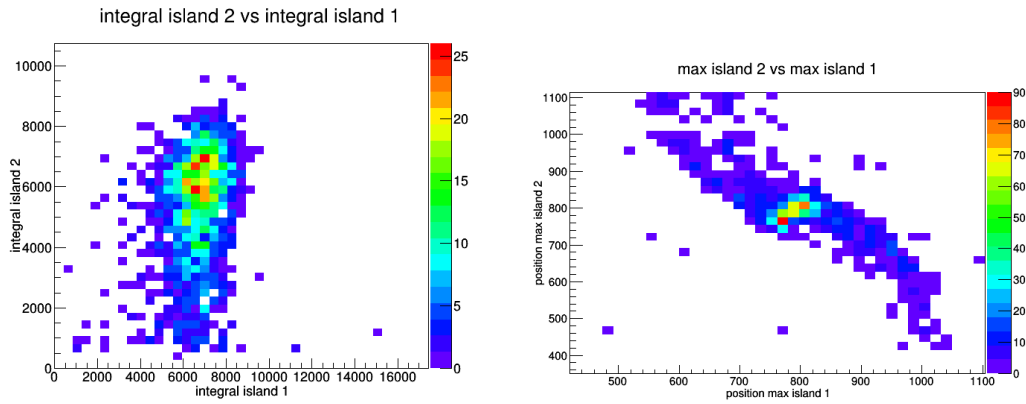


Figure 5.10: The scatter plot of the two integral distribution (left) and the two maximum position distribution.

The gradients on the surface can be calculated in the following way:

$$\nabla_x = \frac{(x - x_{mean}) \cdot c_l}{L \cdot 2} \quad \nabla_y = \frac{(y - y_{mean}) \cdot c_l}{L \cdot 2} \quad (5.1)$$

where x and y are the measured points, x_{mean} and y_{mean} are the mean values extracted from the distribution of the maximum position of Fig. 5.12, c_l is the conversion factor from CCD pixels to mm, L is the distance between aerogel and screen and 2 is a factor due to reflection.

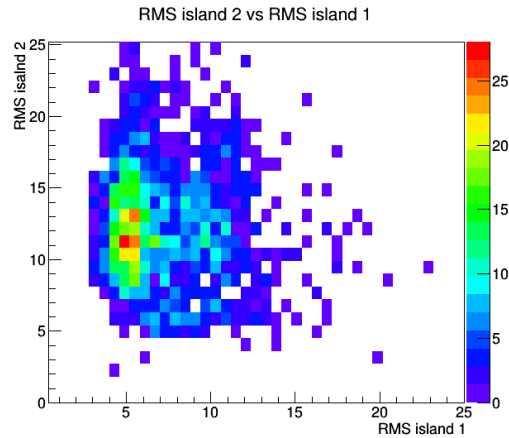


Figure 5.11: The scatter plot of the two RMS distributions.

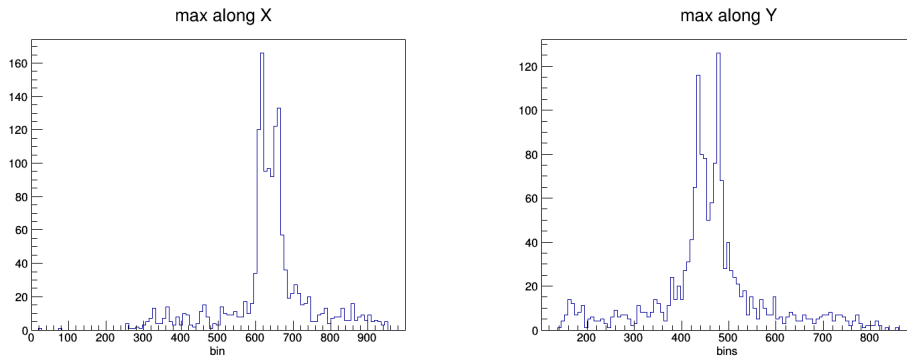


Figure 5.12: The distribution of the maximum along X and Y.

In Fig. 5.13 are shown the the gradients of Face₁. We repeated all the procedure with the aerogel rotated by 180 degrees for the measurements of Face₂. The results are shown in Fig. 5.14. After the calculation of the gradients of both faces, with another software we reconstructed the two surfaces. In this case we are not able to calculate the absolute thickness of the tile since we have only the relative variation of the surface instead of the absolute spatial position. Face₁ and Face₂ are shown in Fig. 5.15.

Comparing the laser reflection measurements with the touching machine ones (Fig. 5.16 for Face₁ and Fig. 5.17 for Face₂) one can verify that looks very similar.

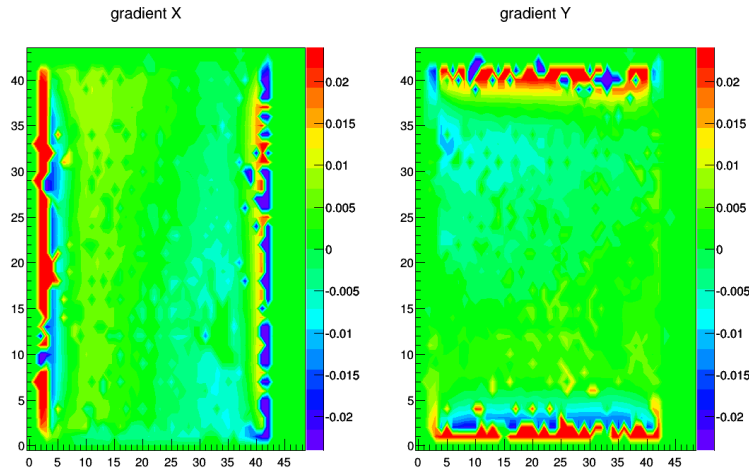


Figure 5.13: The surface gradients ∇_x and ∇_y of the aerogel Face₁ as extracted from the laser reflection technique.

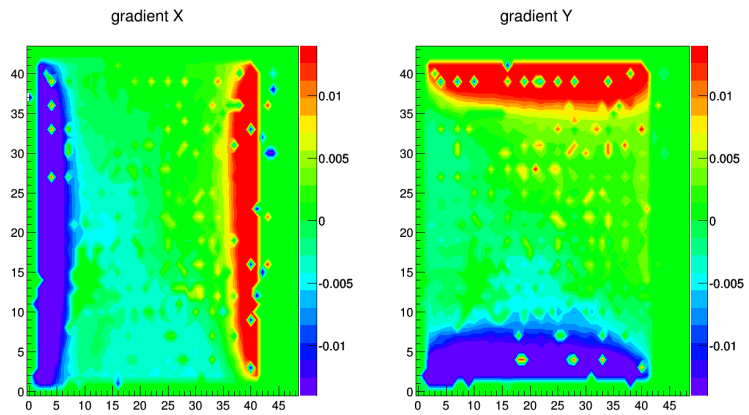


Figure 5.14: The surface gradients ∇_x and ∇_y of the aerogel Face₂ as extracted from the laser reflection technique.

A quantitative way to compare the two images is to plot the distribution of the polar angle of the normals to the surface (θ_{aer}) of the measured points (see Fig. 5.18 and 5.19). The corresponding mean and RMS values are listed in Tables 5.1. The values of the two aerogel faces are compatible. Thus it is possible to conclude the the laser reflection setup, that is a less invasive

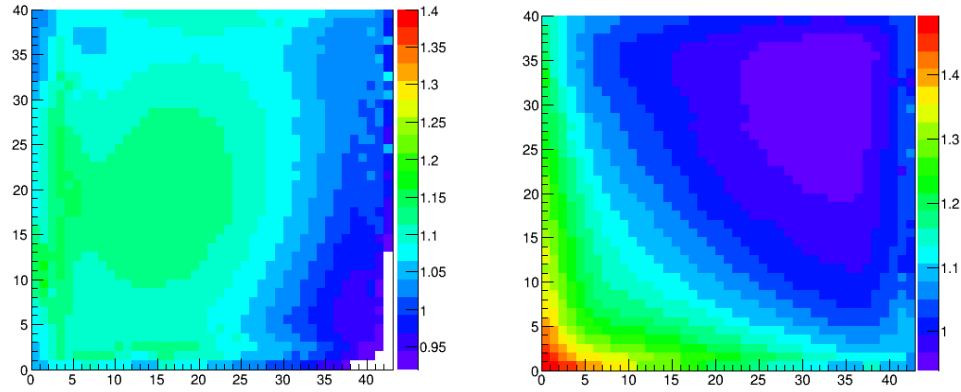


Figure 5.15: As extracted from the laser reflection technique, Face₁ (left) and Face₂ (right).

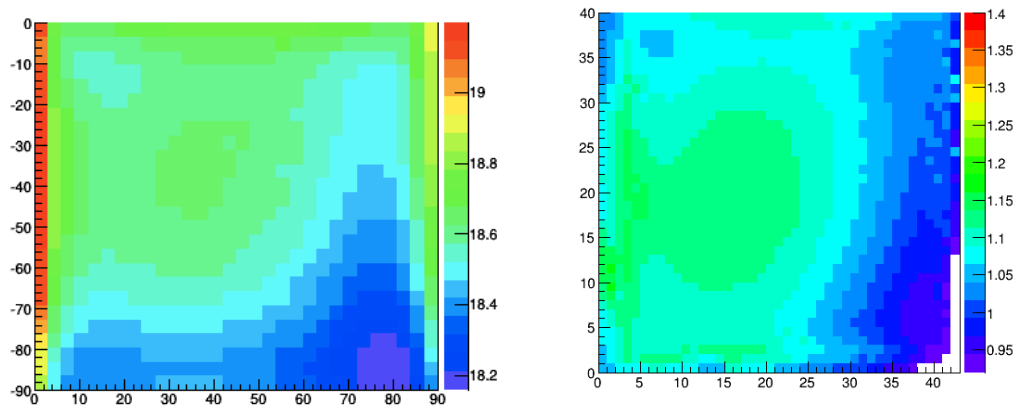


Figure 5.16: The touch machine measurements (left) and the laser setup (right) measurement of the aerogel Face₁ surface shape.

technique, can substitute the touch machine for surface characterization.

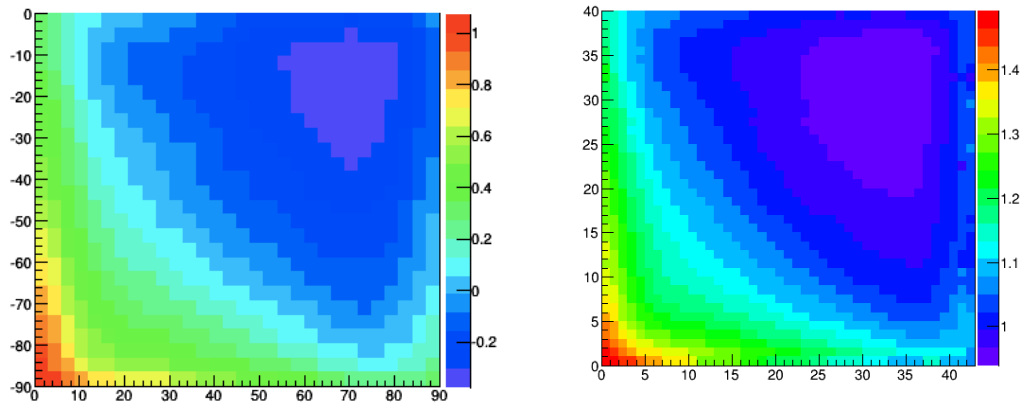


Figure 5.17: The touch machine measurements (left) and the laser setup (right) measurement of the aerogel Face₂ surface shape.

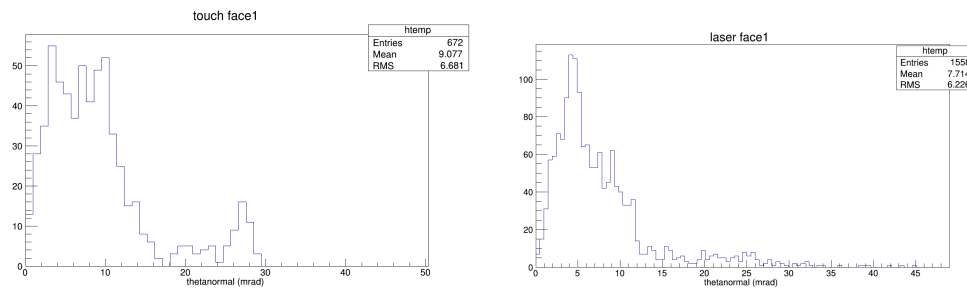


Figure 5.18: The polar angle θ_{aer} distribution of Face₁ as measured by the touch machine (left) and the laser setup (right).

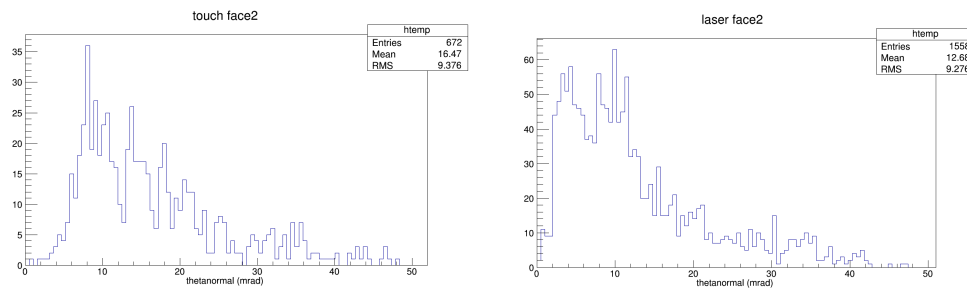


Figure 5.19: The polar angle θ_{aer} distribution of Face₂ as measured by the touch machine (left) and the laser setup (right).

Face ₁	mean _(mrad)	RMS _(mrad)
touch machine	9.08	6.68
laser reflection	7.71	6.23
Face ₂	mean _(mrad)	RMS _(mrad)
touch machine	16.47	9.38
laser reflection	12.68	9.28

Table 5.1

5.3 X-ray Measurement

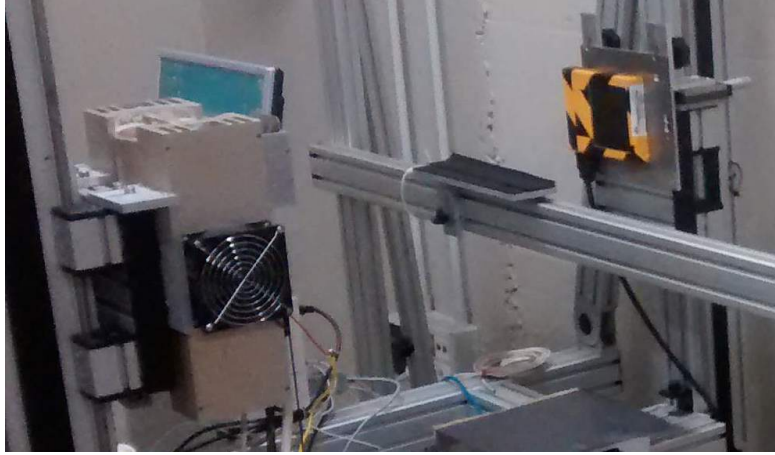


Figure 5.20: The X-ray source and the CMOS detector used for the measurements.

For the X-ray measurement we put the aerogel aligned between the X-ray source and the X-ray detector. We took three kinds of measurement:

- Dark images - X-ray source switched off;
- White images - X-ray source switched on, without aerogel;
- Aerogel images - X-ray source switched on, with aerogel.

We repeated the measurement several times changing various options: X-ray energy, exposition time, number of frames to be averaged. With the obtained data we calculated the attenuation ratio:

$$\mathcal{R} = \frac{A - c_1 D}{cW - c_1 D} \quad (5.2)$$

where A , W and D are respectively the CMOS pixel ADC value of the Aerogel image, White image and Dark image. It is possible to rewrite \mathcal{R} in terms of rate for unit time:

$$\mathcal{R} = \frac{(a + d)\tau_A - c_1 d\tau_D}{c(w + d)\tau_W - c_1 d\tau_D} \quad (5.3)$$

in which a , w and d are the rates per unit time and τ_A , τ_W and τ_D are the exposition times of the Aerogel images, White images and Dark images respectively. If the exposition times are all the same the ratio $\mathcal{R} = a/w$ provides the attenuation due to the aerogel density. The system didn't allow to have always the same exposition time, so the c , c_1 coefficients are needed to synchronize the images. It is possible to synchronize the Aerogel and White images by comparing the integrals of a control region in which there is air in both cases (see Fig.5.21):

$$\tau_A = c\tau_W \Rightarrow c = \frac{\text{Integral}_A}{\text{Integral}_W} \quad (5.4)$$

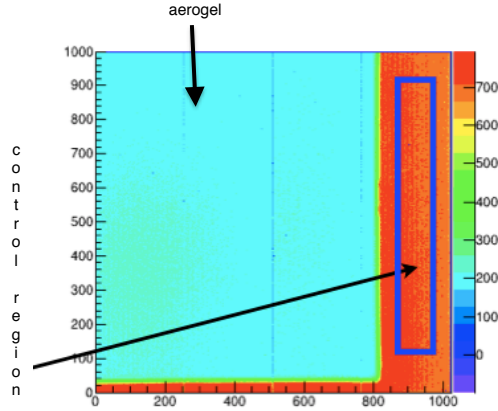


Figure 5.21: The control region used for synchronization.

It's not possible to synchronize the Dark images with a similar method. After the synchronization of A and W images it is possible to estimate the remaining uncertainty σ_τ due to the time synchronization of the Dark image as:

$$\begin{aligned} \sigma_\tau &= \frac{(a+d)\tau_A - d\tau_D}{(w+d)\tau_A - d\tau_D} - \frac{(a+d)\tau_A - d\tau_A}{(w+d)\tau_A - d\tau_A} = \frac{(a+d)\tau_A - d\tau_D}{(w+d)\tau_A - d\tau_D} - \frac{a}{w} = \\ &= \frac{\frac{a}{w} + \frac{d}{w} \left[\frac{\tau_A - \tau_D}{\tau_A} \right]}{1 + \frac{d}{w} \left[\frac{\tau_A - \tau_D}{\tau_A} \right]} - \frac{a}{w} \approx \frac{d}{w} \left[\frac{\tau_A - \tau_D}{\tau_A} \right] - \frac{ad}{w^2} \left[\frac{\tau_A - \tau_D}{\tau_A} \right] \approx \\ &\approx \frac{d}{w} \left[\frac{\tau_A - \tau_D}{\tau_A} \right] \left[1 - \frac{a}{w} \right] \end{aligned} \quad (5.5)$$

where $\frac{d}{w}$ and $\frac{a}{w}$ can be estimated in first approximation with $\frac{D}{W-D}$ and $\frac{A-D}{W-D}$ respectively.

In the table 5.2 it is shown an estimate of the uncertainty assuming a realistic synchronization time error of 10%:

As it shown in the table the best conditions are 25 kV of energy and

Energy _(kV)	D/(W-D)	(A-D)/(W-D)	σ_τ	τ_A (s)	τ_D (s)	τ_W (s)
12	3.3	0.990		45	40	45
15	0.9	0.990		20	25	20
16	12.0	0.197	0.9636	35	35	35
18	4.0	0.200	0.3200	37	40	40
20	1.2	0.290	0.0852	35	35	35
25	0.4	0.437	0.0225	30	30	30

Table 5.2

30 s of exposition time for all the images. Ideally a proper white image normalization and dark count subtraction should remove all the artifacts due to the not-uniform response of the CMOS sensor. The final images still show the structure of the CMOS sensor which is subdivided into four sub-elements. In order to effectively synchronize the dark image, the latter was rescaled by a c_1 factor in order to minimize the artifacts of the image and obtain a smooth variation in the aerogel region (see Fig. 5.25). Different

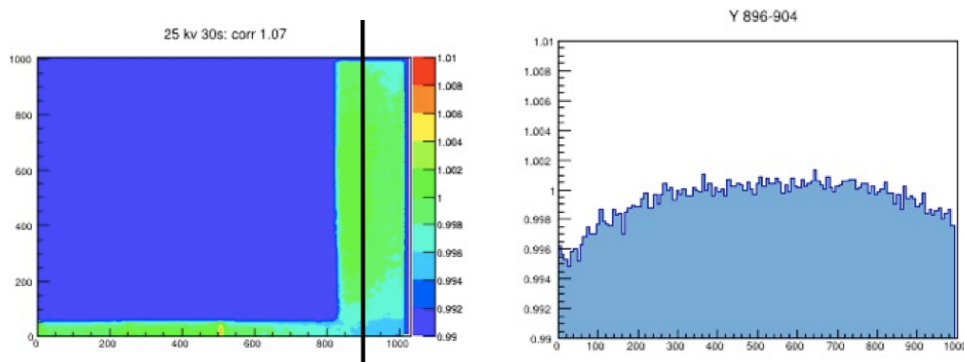


Figure 5.22: The control region after synchronization: the black line indicate the vertical projection shown in the right picture.

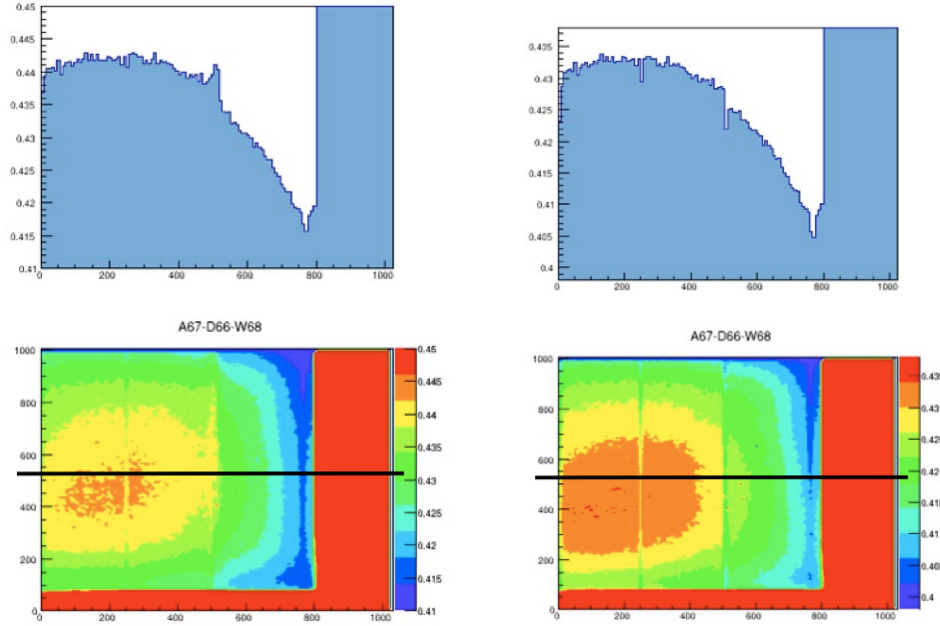


Figure 5.23: \mathcal{R} for $c_1 = 1.07$ (left) and $c_1 = 1.11$ (right). The black line show the bins of the projection.

values of c_1 were tried before choosing the best one. $c_1 = 1.07$ (Fig. 5.23) is too small (as shown by a peak that is present in the projection), $c_1 = 1.11$ (Fig. 5.23) is too big (there is a valley in the same position of the previous peak). The smoothest variation has been found for $c_1 = 1.09$ (Fig. 5.24). Comparing this measurement with the touching machine one (Fig. 5.25) compatible percentage variation are found:

$$\text{x ray : } \frac{0.438 - 0.41}{0.438} = 6.39\%$$

$$\text{touch machine : } \frac{(19.4 - 18.2)\text{mm}}{19.4\text{mm}} = 6.19\%.$$

Therefore the variation seen in x-ray images is mainly due to thickness variation. In order to see density variation further correction are needed. The main problems that need to be solved are time synchronization and air scattering (cause of less defined images respect touch machine measurements).

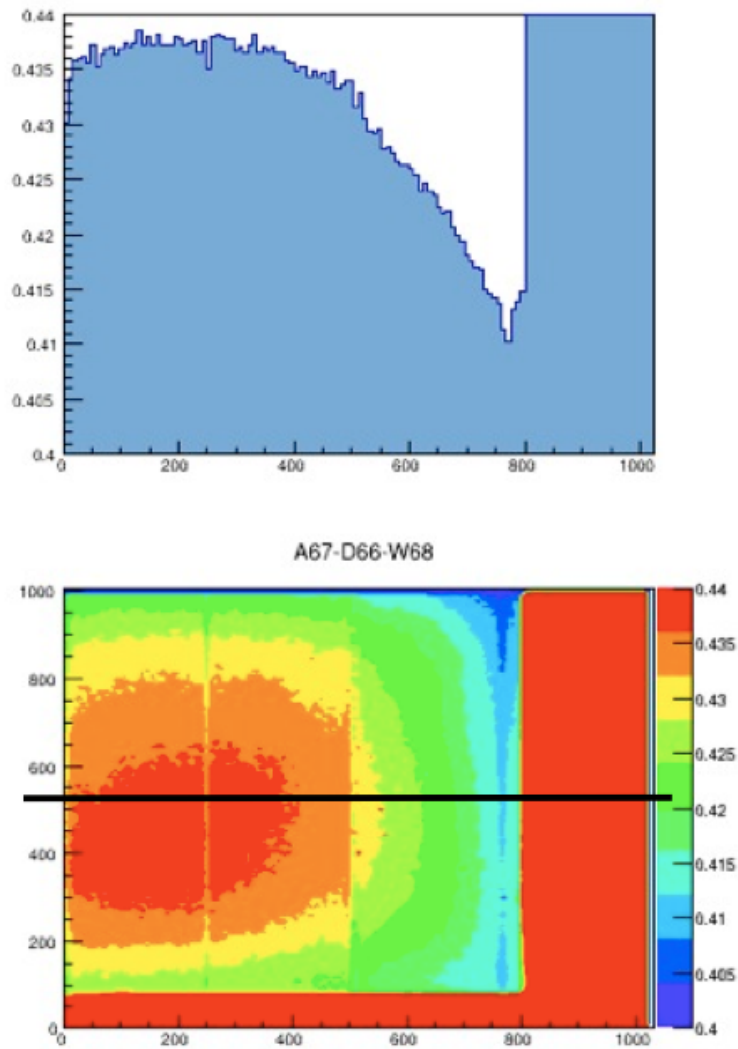


Figure 5.24: \mathcal{R} for $c_1 = 1.09$. The black line show the bins of the projection.

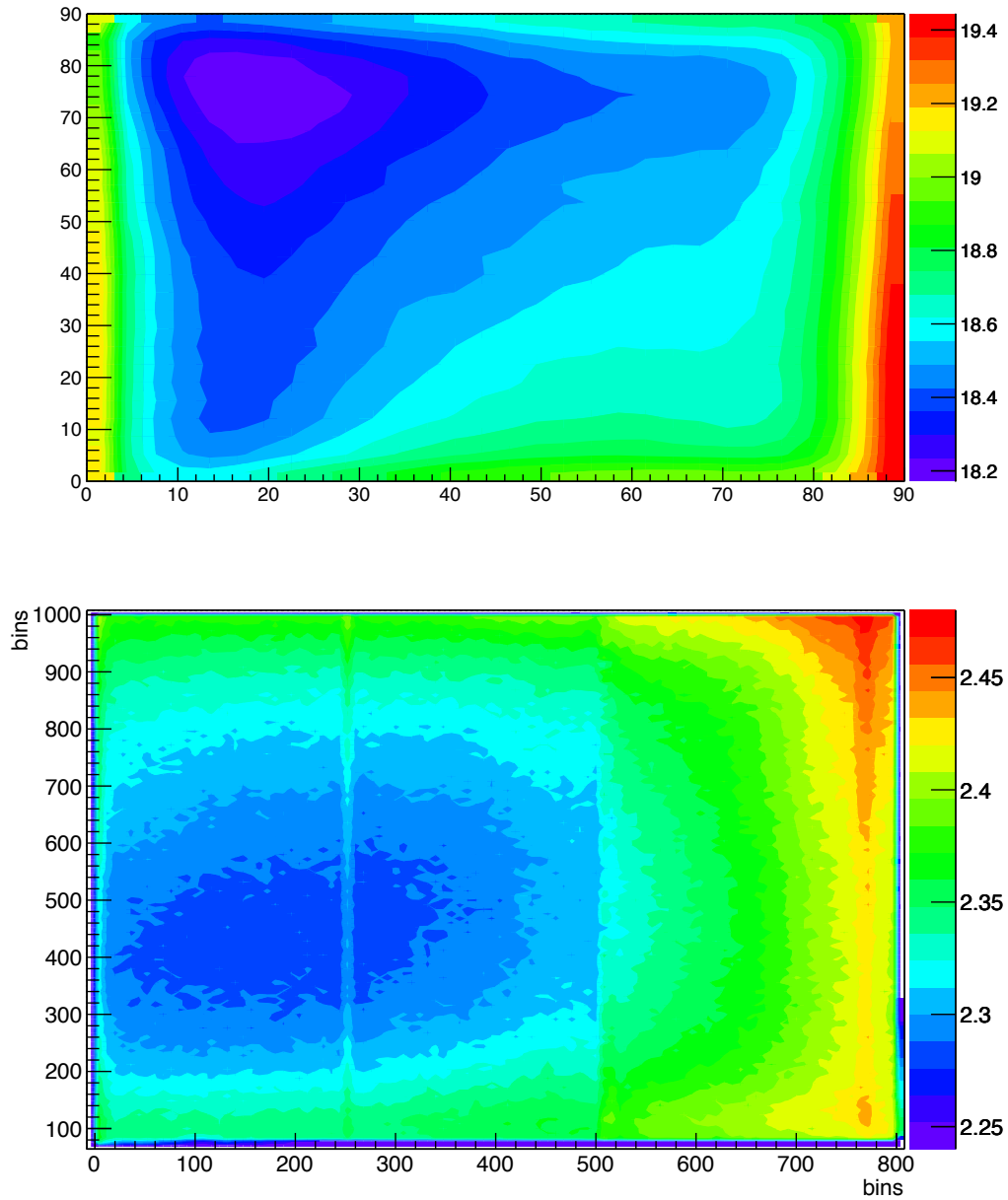


Figure 5.25: Comparison between touch machine (top) and X-ray (bottom) measurement. For having a compatible color scale for the X-ray has been plotted $1/\mathcal{R}$, the inverse of the attenuation ratio.

Chapter 6

Mirror Characterization Measurement

The angular dispersion of the detected Cherenkov photons ($\sigma_{\theta_{Ch}}$) is closely related to the optical properties of mirrors and, in the reflected configuration of the CLAS12 RICH, of the aerogel-mirror system. The number of Cherenkov photons produced by the aerogel is not very large as the refractive index is close to 1 and therefore for a good detector performance is important to optimize the light transportation. Different measurements were done to verify the quality of the spherical mirror demonstrator under different humidity conditions: surface scan and D_0 simulation. The last one in particular gives the possibility to calculate $\sigma_{\theta_{mir}}$, the angular precision of the mirror. The aim of the aerogel-mirror system measurement was to quantify the angular dispersion ($\sigma_{\theta_{Ch}}$) of the reflected laser beam due to the aerogel tile surface imperfection ($\sigma_{\theta_{aer}}$).

6.1 Mirror Measurement

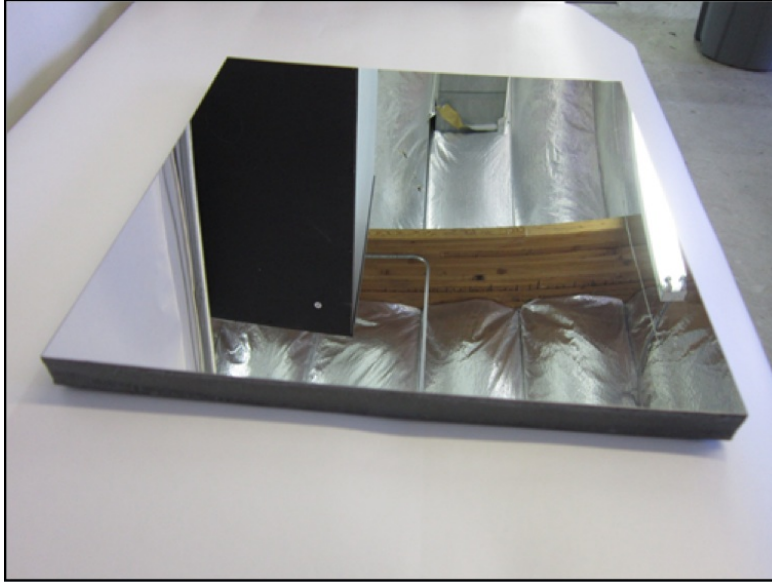


Figure 6.1: The mirror demonstrator.

A spherical mirror demonstrator was delivered by the CMA company of Tucson, AZ, USA. It is a square of 30 cm side and a 3500 mm nominal radius with a maximum allowed peak-to-valley variation of $2.5 \mu\text{m}$. Various surface scans have been done from September to December 2014 with the touching machine for testing locally the mirror quality. Each time two staggered measurement (hereinafter PL2 and PL3) were done in order to obtain higher number of measured points. 929 points has been measured in PL2 and 899 in PL3 measurements all respect the same coordinate system (see Fig. 6.2). The origin of the reference frame is in the bottom left corner of the mirror. PL2 first point is distant 3 mm in X and 3 mm in Y from the origin, instead PL3 first point is distant 8 mm in X and 3 mm in Y . The step between two adjacent points is 10 mm. Each measurement provides the spatial point XYZ coordinates respect the reference frame. PL2 and PL3 data have been processed with a maximum likelihood fitting software to extrapolate the center position and the curvature radius of the spherical mirror. Then the difference δr between real and ideal mirror shape has been computed by means of the

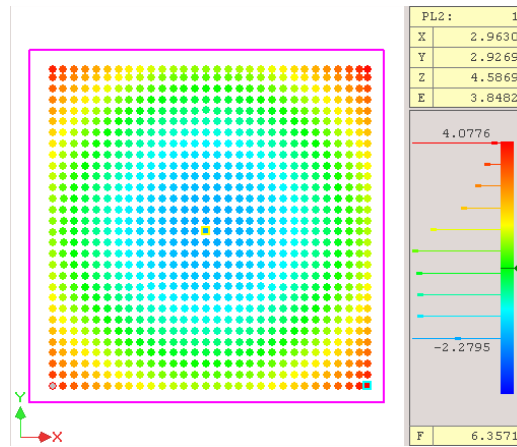


Figure 6.2: The reference frame of the measurement.

obtained parameters:

$$\delta r = \sqrt{(x - x_0)^2 + (y - y_0)^2 + (z - z_0)^2} - r \quad (6.1)$$

where x , y and z are the measured coordinates, x_0 , y_0 , z_0 are the coordinate of the center and r the radius obtained with the maximum likelihood fit. The results has been plotted in a 2D histogram (showing the variation point by point) and a 1D histogram (showing the dispersion of the values). An example of the two histograms is shown in Fig. 6.3. Using the PL2 and PL3 data, it has been possible to simulate the D_0 (Fig. 6.4) and $\sigma_{\theta_{mir}}$, two global estimators of the mirror quality described in the following. The image of an object at the center of curvature of a spherical mirror is reflected in the same position (center of curvature) and has ideally the same size. So the image of a point-like light source reflected by an ideal mirror is again point-like. Instead, a real mirror will produce a spot with a finite dimension, due to its imperfections. The D_0 parameter is defined as the diameter of the circle, at the mirror center of curvature, containing 95% of light reflected by a spherical mirror illuminated by a point-like source positioned in the center of curvature. If the light distribution is gaussian, its standard deviation σ_s and the parameter D_0 are linked by a simple relation:

$$\sigma_s = \frac{D_0}{4}. \quad (6.2)$$

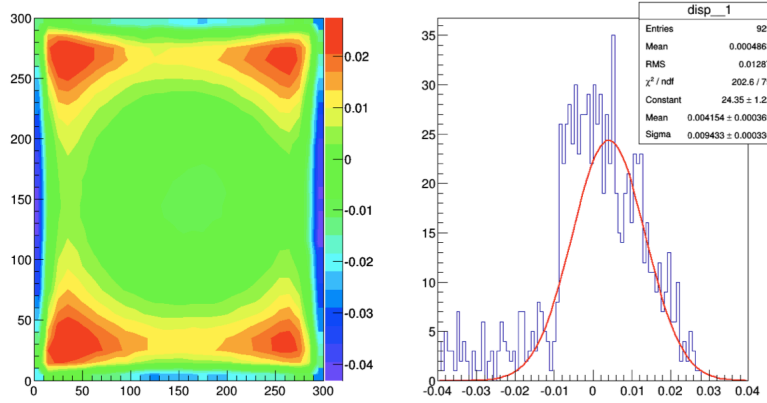


Figure 6.3: The mirror deviation δr from the ideal spherical surface: 2D point-by-point histogram (left) and the 1D dispersion histogram (right).

Measuring D_0 is possible to determine the RMS of the angular deviation of the normal to the mirror surface $\sigma_{\theta_{mir}}$, i.e.:

$$\sigma_{\theta_{mir}} = \frac{\sqrt{\sigma_s^2 - \sigma_p^2}}{2r} \sim \frac{\sigma_s}{2r} = \frac{D_0}{8r} \quad (6.3)$$

where σ_p is the point-like source actual dimension, which we consider negligible. With a ray-tracing simulation it has been possible to calculate the D_0 (and therefore the $\sigma_{\theta_{mir}}$) of the mirror demonstrator using the touching machine measurement.

The first surface measurement of the mirror demonstrator was done by the CMA manufacturer company with a Shack-Hartmann wave-front sensor. As shown in Fig. 6.5 they found a peak-to-valley value of $1.86 \mu m$ and an RMS of the deviations from the ideal spherical surface of $0.38 \mu m$. In the months between September and December the mirror has been exposed to different levels of humidity (from 0 up to 80%) for studying shape deformations.

Various graphs have been done showing the variation of radius (Fig. 6.6), surface imperfection RMS (Fig. 6.7) and D_0 (Fig. 6.8) of the mirror demonstrator. In each graph the measurement of the total surface and of the central area (without 5 cm on each side) are presented.

As shown in Table 6.1 the range of $\sigma_{\theta_{mir}}$ is from 0.1 up to 0.16 mrad. It corresponds to a $\sigma_{\theta_{Ch}}^{spherical}$ range from 0.13 up to 0.21 mrad, that is inside the

total surface						
date	humidity (%)	radius (mm)	peak-to-valley (μm)	RMS (μm)	D_0 (mm)	$\sigma_{\theta_{mir}}$ (mrad)
Sep.		3485.7	70	12.9	4.4	0.16
		3494.7	48	9.8	3.7	0.13
31 Oct.	30 - 35	3492.7	46	8.8	3.5	0.13
		3498.2	33	7	3.3	0.12
6 Nov.	0	3494.7	36	6.6	3	0.11
		3497.6	29	5.5	2.7	0.10
17 Nov.	50 - 80	3494.1	59	12.4	4.3	0.15
		3497.5	41	8.4	3.4	0.12
1 Dic.	0	3498.1	29	4.8	2.6	0.09
		3503.4	24	4.8	3.2	0.11
central area						
Sep.		3514.6	6.4	1.2	1.5	0.05
		3516.7	6.4	1.3	1.6	0.06
31 Oct.	30 - 35	3514.2	5.3	1.1	1.4	0.05
		3516.8	8.2	1.6	1.9	0.07
6 Nov.	0	3512.6	5.7	1	1.3	0.05
		3513.1	5.6	1.2	1.4	0.05
17 Nov.	50 - 80	3520.4	8.2	1.5	2.4	0.09
		3520.1	5.7	1.1	1.5	0.05
1 Dic.	0	3520.0	7.5	1.7	2.2	0.08
		3520.0	7.6	1.6	2.1	0.07

Table 6.1: For each date top line is PL2, bottom line is PL3

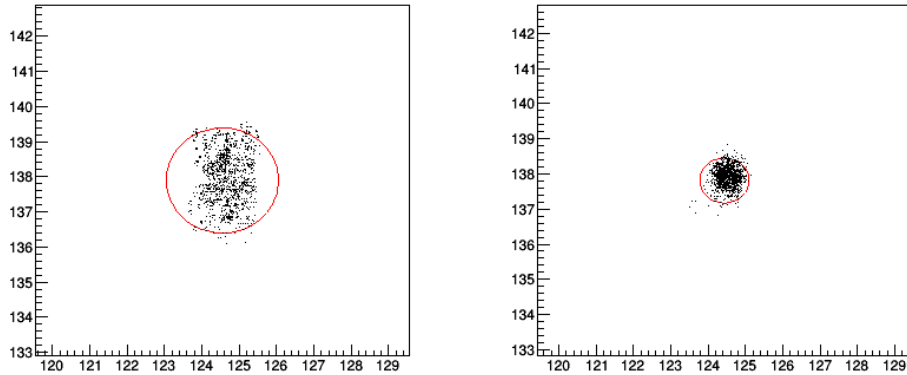


Figure 6.4: The distribution of the simulated light ray reflections by the CMA spherical mirror demonstrator and the D_0 area in red: on the left of the total surface, on the right of the central area.

constraints calculated in Chapter 4. However, as shown from all the graphs, in all the measurement (done from September to December 2014) the quality of the demonstrator was lower of that measured by CMA (on April 2014). Peak-to-valley and RMS were bigger in every measured condition and CMA values were never reached.

The biggest variation were on the edges of the demonstrator, as shown by the higher variation of the measurements of the total surface with respect the central area ones.

Although RICH detector will be operated in a dry nitrogen environment, it was useful to study the behavior of the mirror demonstrator under different humidity conditions to test the rigidity of the mirror structure. These measurements show that the foam core of the demonstrator is not rigid enough to resist to the epoxy glue shrinkage and to humidity changes and therefore can not be stored or handled in normal atmosphere. This also indicates that the foam core is not stiff enough to prevent deformations due to the long-term epoxy glue shrinkage, the most likely reason for the deterioration of the mirror from the initial measurement done at CMA and the 6 months later performed during the thesis work.

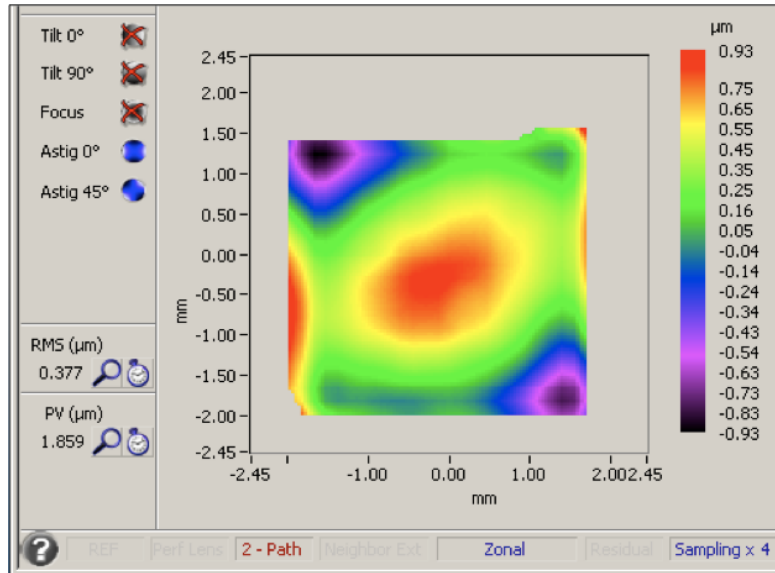


Figure 6.5: The CMA surface measurement done with a Shack-Hartmann sensor.

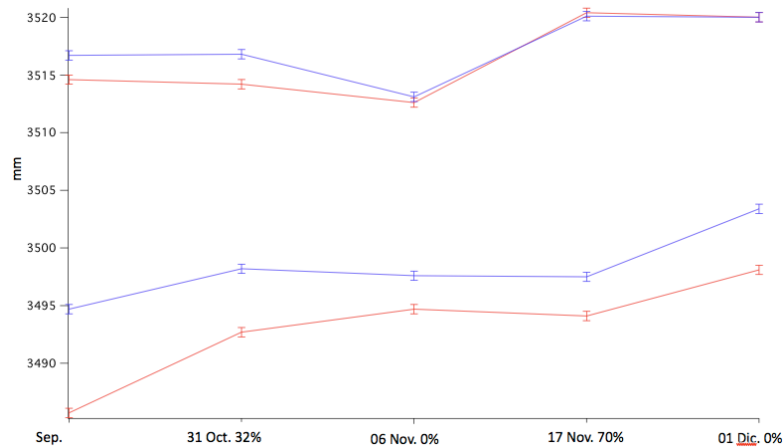


Figure 6.6: Radius variation during the stress tests (red PL2, blue PL3). On top the central area of the mirror. In the bottom the total surface.

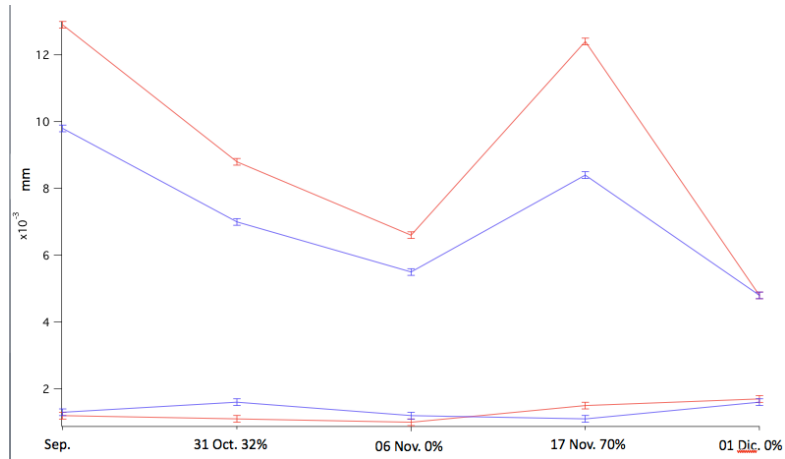


Figure 6.7: Surface variation RMS variation during the stress tests (red PL2, blue PL3). On top the total surface. In the bottom the central area.

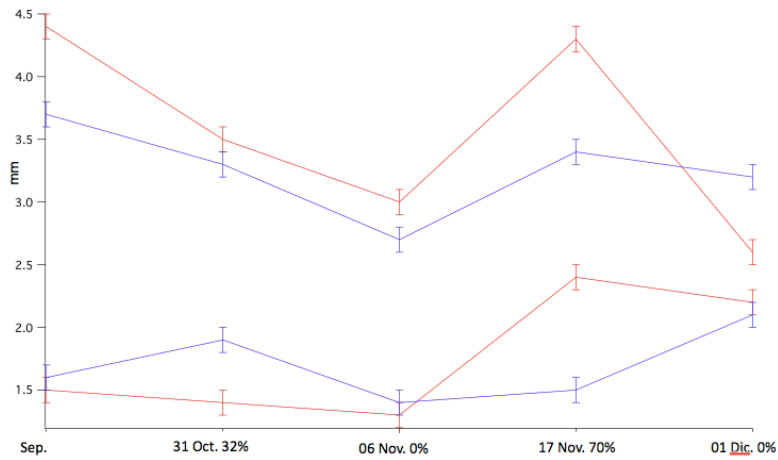


Figure 6.8: D_0 variation during the stress tests (red PL2, blue PL3). On top the total surface. In the bottom the central area.

6.2 Planar Mirror Measurement

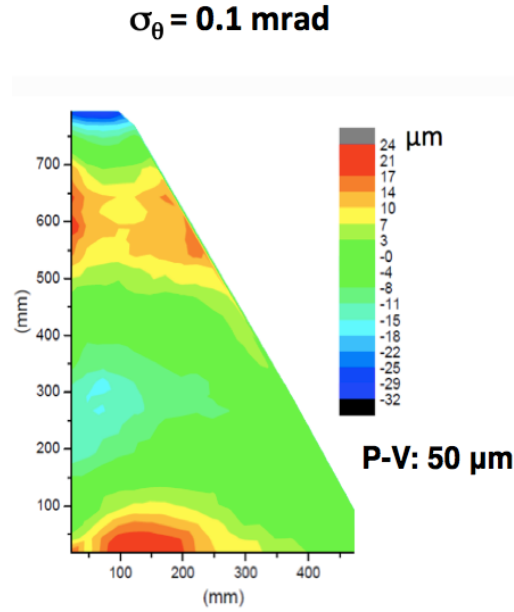


Figure 6.9: The planar mirror measurement.

A real size planar mirror demonstrator was delivered by the Media-Lario company of Bosisio Parini, Italy. The surface quality, as measured by a touching machine by the company, is shown in Fig. 6.9. The measured $\sigma_{\theta_{mir}}$ is 0.1 mrad and the peak-to-valley is 50 μm . The corresponding $\sigma_{\theta_{Ch}}^{planar}$ is 0.06 mrad. Therefore the main contribution to $\sigma_{\theta_{Ch}}^{focus}$ is the aerogel one.

6.3 Aerogel-Mirror Measurement

The aim of this measurement was to quantify the enlargement of a laser beam ($\sigma_{\theta Ch}$) after the multiple refraction through an aerogel tile plus the reflection from a planar mirror. The main contribution is from the aerogel, since of the high quality of mirror used in the experiment. With the equation 4.16 and 4.17 of the Chapter 4 and the aerogel surface scan shown in Chapter 5 it is possible to simulate the laser beam behavior. Assuming an aerogel surface error $\sigma_{\theta_{aer}}$ of 9 mrad (the worst of the two measured, see Fig. 5.19) the beam dispersion in function of the impinging laser angle has been calculated. The results are shown in Fig. 6.10: the light dispersion $\sigma_{\theta_{light}}$ due to the aerogel

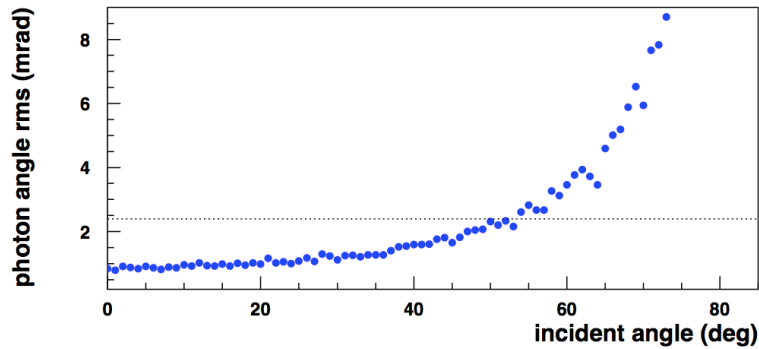


Figure 6.10: The dispersion of the laser beam $\sigma_{\theta_{light}}$ after 2 passages through the aerogel respect the angle on incidence. For comparison, the horizontal dashed line represent the angular spread due to the RICH photodetector (in mrad).

surface imperfections is acceptable (comparable to the RICH pixel contribution) up to 50° (a value bigger enough with respect the mean Cherenkov angle). A much more useful quantity that can be computed (using the same equation and the same data) is the ratio between $\sigma_{\theta_{light}}$ and the aerogel $\sigma_{\theta_{aer}}$ as a function of the impinging laser angle. This quantity correlates the light spot enlargement to the surface quality of the aerogel. In this way it is possible to put a limit on the aerogel surface quality, i.e. setting the maximum angular dispersion value $\sigma_{\theta_{aer}}$ for the aerogel acceptance tests. The results are shown in Fig. 6.11.

In Fig. 6.12 is shown the setup used aerogel-mirror reflection measurement.

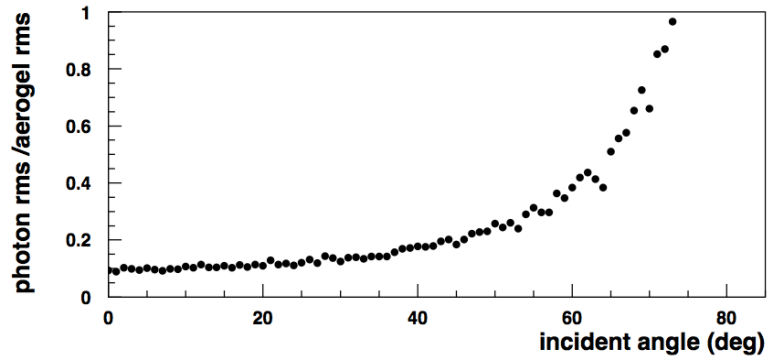


Figure 6.11: The ratio between light angular dispersion $\sigma_{\theta_{light}}$ and surface aerogel angular dispersion $\sigma_{\theta_{aer}}$ as a function of the angle of incidence.

A helium-neon ($\lambda = 632.8$ nm) laser sent the beam at an approximate angle

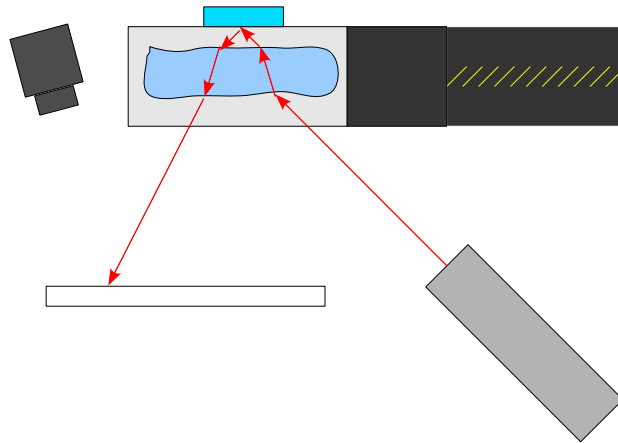


Figure 6.12: The aerogel-mirror reflection scheme.

of 45° in the horizontal plane respect the surface of the aerogel. The aerogel is on an holder attached to two step motors for movement in XY-plane. Behind the aerogel tile is placed an high-quality planar mirror. A white screen is in front of the aerogel, shifted so as to intercept the reflected beam. In front of the screen there is a CCD camera. First measurement was done

without aerogel (only the mirror) in order to have a reference. Differently from previous measurement, in this case it has not been possible to scan the whole aerogel surface, due to the laser beam path inside the aerogel. The intensity of the transmitted light spot is high enough to require a light attenuator in order not to saturate the CCD camera signal. As a consequence, the reflected light spots from the aerogel surface are too faint to be recorded. All the data of the reflected laser spot were collected using the software developed for aerogel characterization and stored in a ROOT tree. In Fig. 6.13

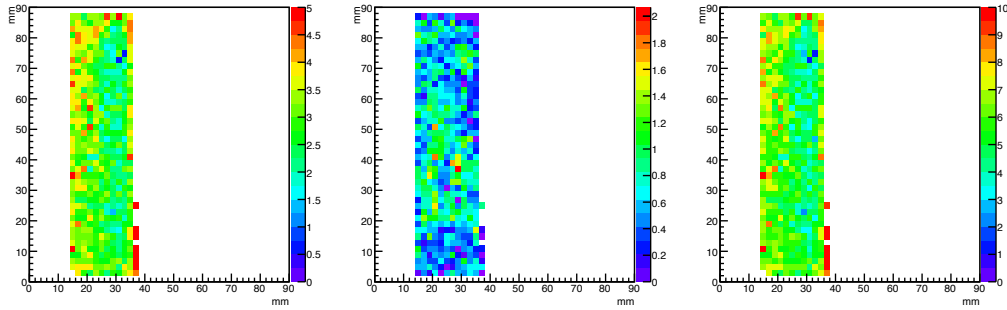


Figure 6.13: On the left the shift of the spot maximum respect the reference. In the center the spot RMS. On the right the beam deviation in mrad.

the results are shown. The mean value and the RMS of the laser spot are:

$$\text{mean} : 5.71 \text{ mrad} \quad \text{RMS} : 1.44 \text{ mrad}$$

In Table 6.2 these values are compared with the surface aerogel aerogel surface angular dispersion (of the same measured region, see Fig. 6.14).

The two ratios are compatible with each other and even more the are com-

	mean _{mrad}	RMS _{mrad}
laser spot	5.71	1.44
aerogel surface	17.21	4.65
ratio	0.33	0.31

Table 6.2

patible with the value shown in the graph 6.11 for 55° , close enough to the

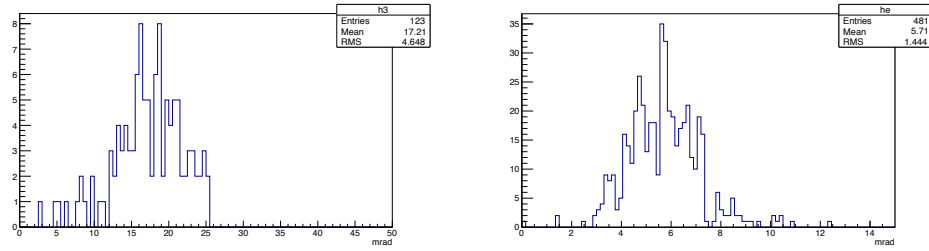


Figure 6.14: The polar angle θ_{aer} distribution of the aerogel surface (left) and the laser spot angular distribution θ_{light} (right). The measurements are done in the same aerogel area.

nominal angle of the measurement. Therefore, using as a reference the angular spread due to the RICH photodetector, the maximum value for $\sigma_{\theta_{aer}}$ is:

$$\sigma_{\theta_{aer}} = \frac{2.45 \text{ mrad}}{0.31} = 7.9 \text{ mrad}$$

Chapter 7

Conclusion

The main subject of this thesis work is the CLAS12 Ring Imaging Cherenkov detector. CLAS12 RICH is a dual mode detector. It collects light either directly or after reflection by the focusing system. In the last case the aerogel tiles are thick (6 cm) and the emitted photons (after been reflected by the spherical mirror) have to pass through the thinner tiles (2 cm) before reaching the PMTs. So the focusing system optical properties are crucial for the RICH efficiency. The aim of the thesis work has been the study of all the contribution to the single photon resolution of the focusing system $\sigma_{\theta_{Ch}}^{focus}$ and the development of a not-invasive measurement protocol to study in detail the relevant aerogel properties, in particular the angular distribution of the normal to the aerogel surface θ_{aer} . Several method for the aerogel characterization were presented: x-ray radiographic technique, touching machine surface scan, laser reflection setup. For each of them a specific software was developed for the data-analysis. The Japanese BTR 12-3a aerogel tile was used as sample test in all the measurements, being hydrophobic (not sensitive to the ambient humidity). The purpose of x-ray radiographic technique was to measure local refractive index inhomogeneities. Plots presented in Chapter 5 are consistent with the thickness measurements done with the touching machine. Therefore the inhomogeneities seen in the graphs are mainly a thickness effect and currently it is not possible to isolate refractive index variations. Further studies are requested to make this technique suitable. The surface measurements were done with the touching machine

and the laser reflection setup. The touching machine gives good results but it is quite invasive (touching the aerogel could ruin the surface). The laser reflection setup gives result compatible with the touching machine, thus can substitute it. Applying the laser reflection technique to the aerogel-mirror system it was possible to derive an upper limit on the aerogel surface quality:

$$RMS_{\theta_{aer}} < 7.9 \text{ mrad}$$

If the RMS of the angular distribution of the normal to the aerogel surface is smaller than 7.9 mrad, the tile is suitable for the CLAS12 RICH. Finally a spherical mirror demonstrator was measured with the touching machine for testing the rigidity of the Carbon-Fiber Reinforced Polymer (CFRP) structure, sandwiching a 25 mm core of rohacell foam. The foam was sensible to different humidity condition, showing big variation in the measured curvature radius and the RMS of the difference between real and ideal mirror shape, in particular on the edges. A new technology of carbon-fiber honeycomb will be tested in the future.

Appendix A

Large Area Picosecond PhotoDetector



Figure A.1: The LAPPD sample number 28.

During an internship at Jefferson Lab some tests on new Large-Area Picosecond Photo-Detectors has been done as part of the R&D studies for the RICH of the future Electron-Ion Collider (EIC). The main goal of this activity is the development of cheap, large area, single photon detector, based on the Micro Channel Plate technology. The RICH group collaborate with LAPPD activity because cheap detector could eliminate the requirement of the focusing configuration. In particular, the mean number of photoelectrons produced in function of the rate of the incident photons was measured and the Quantum Efficiency of the detector was evaluated. As shown in Fig. A.2

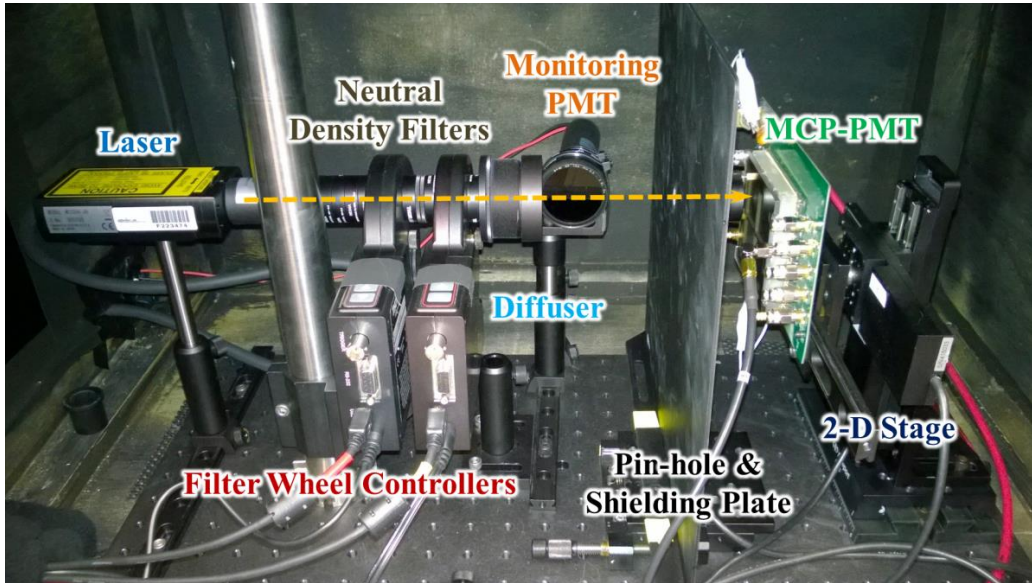


Figure A.2: The darkbox where was done the measurements.

the measurement was done with a Hamamatsu picosecond light pulser (PLP-10) with a central wavelength at 405 nm (it has an average 60 ps pulse width and the repetition rate can go up to 100 MHz). The setup was completed by two neutral density filter wheels for laser beam attenuation, a pin-hole design to limit the laser spot to be less than 2 mm and a 2-D moving stage with a travel of 5 cm in both X and Y directions. Another fast PMT was installed in the dark box to monitor the light yield and it can also be used as a source of trigger. The first measurement was the study of the mean number of observed photoelectrons as a function of the frequency of laser pulses. First of all of the

gain at 2500 V was measured, setting the system at the single photo-electron level, resulting of 1.1×10^6 . Then the light intensity was set to a multi-photon level and various laser frequency were tested. All the measurement were repeated at 50% of light intensity. For each laser frequency, with the measured gain the mean number of detected photoelectrons was extracted from the charge spectrum after pedestal subtraction. The results are shown in Fig. A.3.

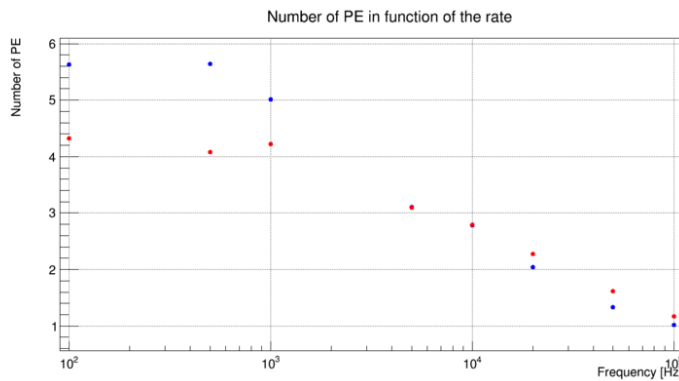


Figure A.3: Rate measurements: blue dots are measurements at high photon level, red dots are measurements with the 50% filter.

The next measurements allowed the Quantum Efficiency evaluation. With a photodiode the incident photon flux was monitored, measuring the photodiode current as a function of the frequency of laser pulses. Then dividing the fraction of events above the pedestal (calculated with the previous measurement data) over the number of the incident photons the Quantum Efficiency was obtained. The results are shown in Table A.1.

Voltage(V)	Q.E. %
2400	0.18
2600	1.7
2800	1.98

Table A.1

The obtained results are not very satisfactory and further studies and developments are needed.

Bibliography

- [1] Ashman, J.; et al. (EMC Collaboration) (1988). "A measurement of the spin asymmetry and determination of the structure function g_1 in deep inelastic muon-proton scattering".
- [2] Burkardt, M. et al "Spin-polarized high-energy scattering of charged leptons on nucleons " Rep. Prog. Phys. 73 016201, (2010)
- [3] HERMES, A. Airapetian et al., Phys. Lett. B666 (2008) 446, 0803.2993.
- [4] M. Contalbrigo, Overview of Experimental Results from HERMES, International Journal of Modern Physics: Conference Series
- [5] M. Contalbrigo, TMDs and Unpolarized SIDIS, EPJ Web of Conferences
- [6] P. Aguayo et al., NIMA 560 (2006) 291
- [7] R. De Leo et al., NIMA 457 (2001) 52
- [8] M. Tabata et al., X-ray radiographic technique for measuring density uniformity of silica aerogel
- [9] A.F. Danilyuk et al., Recent results on aerogel development for use in Cherenkov counters
- [10] G. Angelini, Characterization of the mirror focusing system for the CLAS12 RICH
- [11] M. Contalbrigo et al., " The large-area hybrid-optics CLAS12 RICH detector: Tests of innovative components" , Nucl. Inst. and Meth. (2014).

- [12] A. R. Montgomery, "A ring imaging Cherenkov detector for CLAS12", *Nuc. Inst. and Meth.* Volume 732, 21 December 2013, Pages 366–370.
- [13] T. Bellunato et. al., *Eur. Phys. J. C* 52 (2007) 759-764.
- [14] Hamamatsu, "Photomultiplier Tubes. Basics and Applications", Third Edition (3a), 2007, pag. 252.
- [15] M. Hoek et al., "Investigation of Hamamatsu H8500 phototubes as single photon detectors."- arXiv:1409.3622
- [16] E. Nappi, J. Seguinot, DOI 10.1393/ncr/i2006-10004-6